KfK 4318 B
Oktober 1987

# Nuclear Moments and Isotopic Variation of the Mean Square Charge Radii of Strontium Nuclei by Atomic Beam Laser Spectroscopy

S. Chongkum
Institut für Kernphysik

Kernforschungszentrum Karlsruhe

KERNFORSCHUNGSZENTRUM KARLSRUHE

Institut für Kernphysik

KfK 4318 B

# NUCLEAR MOMENTS AND ISOTOPIC VARIATION OF THE MEAN SQUARE CHARGE RADII OF STRONTIUM NUCLEI BY ATOMIC BEAM LASER SPECTROSCOPY *

Somporn Chongkum

Kernforschungszentrum Karlsruhe GmbH, Karlsruhe

* von der Fakultät für Physik an der Universität Fridericiana Karlsruhe (TH) genehmigte Dissertation

Kernforschungszentrum Karlsruhe GmbH
Postfach 3640, 7500 Karlsruhe 1

ISSN 0303-4003

# NUCLEAR MOMENTS AND ISOTOPIC VARIATION OF THE MEAN SQUARE CHARGE RADII OF STRONTIUM NUCLEI BY ATOMIC BEAM LASER SPECTROSCOPY

## ABSTRACT

Hyperfine structure and optical isotope shift measurements have been performed on a series of stable and radioactive strontium isotopes ($A = 80$ to $90$), including two isomers 85m and 87m. The spectroscopy applied continuous wave dye laser induced fluorescence of free atoms at $\lambda = 293.2$ nm in a well collimated atomic beam. The 293.2 nm ultraviolet light was generated by frequency doubling the output of a dye laser in either a temperature tuned Ammonium Dihydrogen Arsenate ( ADA ) crystal or an angle tuned Lithium Iodate crystal. A special radio frequency (rf) technique was used to tune the dye laser frequency with long term stability. Radioactive Sr isotopes were produced either by neutron capture of stable strontium or by ($\alpha$,xn) reactions from krypton gas. The samples were purified by an electromagnetic mass separator and their sizes were of order 100 pg, which corresponds to $10^{11}$ atoms. The observed results of the hyperfine structure components are evaluated in terms of nuclear magnetic dipole moments and electric quadrupole moments. Changes in mean square charge radii of strontium nuclei which were extracted from the isotope shift measurements, exhibit a distinct shell effect at the neutron magic number $N = 50$. The experimental data are analysed and compared with some theoretical nuclear model predictions. The strong increase of the nuclear charge radii with decreasing neutron number of isotopes below $N = 50$ is in agreement with the variation of the mean square deformation extracted from measured B(E2) values.

# KERNMOMENTE UND VARIATION DER MITTLEREN QUADRATISCHEN LADUNGSRADIEN DER STRONTIUM–KERNE AUS DER ATOMSTRAHL-LASERSPEKTROSKOPIE

## ZUSAMMENFASSUNG

Die Hyperfeinstruktur und die optische Isotopieverschiebung wurden an einer Reihe von stabilen und radioaktiven Strontium-Isotopen ($A=80$ bis 90) und den beiden Isomeren 85m und 87m untersucht. Die verwendete spektroskopische Methode war die Laserspektroskopie an freien Atomen eines gut kollimierten Atomstrahls, wobei der Übergang SrI 293.2 nm angeregt wurde. Das 293.2 nm UV-Licht wurde durch Verdopplung der Frequenz des Lichts eines frequenzveränderlichen Farbstofflasers erzeugt. Die Verdopplung fand entweder in einem temperaturgetunten ADA-Kristall oder in einem winkelgetunten $LiIO_3$-Kristall statt. Die Laserfrequenz wurde mittels einer speziellen Hochfrequenztechnik durchgestimmt, mit der eine hohe Langzeitsstabilität der Frequenz des Farbstofflasers erreicht wurde. Die radioaktiven Sr-Isotope wurden entweder durch Neutroneinfangreaktionen an stabilen Strontium-Isotopen oder durch $(\alpha,xn)$-Reaktionen an einem Kryptongas-Target produziert. Die Proben wurden durch einen elektromagnetischen Massentrenner gereinigt; die so erhalten Mengen waren von der Grössenordnung 100 pg, das sind $10^{11}$ Atome. Die experimentellen Daten wurden analysiert und mit verschiedenen theoretischen Kernmodellen verglichen. Aus den gemessenen Hyperfeinstruktur-Komponenten konnten die magnetischen Dipolmomente bestimmt werden. Die Änderungen der mittleren quadratischen Kernladungsradien, die aus den Isotopieverschiebungen abgeleitet wurden, zeigen den Effekt des Abschlusses der Neutronenschale am Kern mit $N = 50$. Die starke Zunahme der Kernladungsradien mit abnehmender Neutronenzahl unterhalb $N = 50$ ist in Übereinstimmung mit der Änderung der mittleren quadratischen Kerndeformation, die man aus gemessenen B(E2)-Werten erhält.

# CONTENTS

# 1. INTRODUCTION

The changes in sizes of the nuclear charge distribution between isotopes of an element can be determined from isotope shift (IS) measurements in atomic spectra. In addition, the hyperfine structure (hfs) provides information concerning nuclear moments and electronic structures as described in detail by Kopfermann /Kop.58/.

The optical isotope shifts in atomic spectra are often within the frequency range of megahertz (MHz) to gigahertz (GHz). Compared to the visible light of frequency $10^{14}$ Hertz, such a small shift should be measured by a method with the highest possible resolution. The laser spectroscopic technique is a very precise method and proper for this purpose /Dem.80/. Sensitivity and precision are two particular features of the experiment. The great sensitivity of the optical techniques allows the spectroscopy of minute samples of natural isotopes, isomers and also radioactive isotopes. In addition, the better precision of measurement enables one to develop the theoretical aspect with more confidence.

In a program to study systematically nuclei on both sides of the stability line /Reb.82/, measurements of isotope shifts and the hyperfine structures of a long sequence of the strontium isotopes from mass number A = 80 up to A = 90 by using a high resolution atomic beam laser spectroscopy are reported.

Strontium (Z=38) is an alkaline earth element in which the electronic configuration of states is characterized by two valence electrons outside a closed electron core. The nuclear structure is composed of protons at $2p_{3/2}$ full subshell configuration and the neutron configuration lies between $1g_{9/2}$ and $2f_{5/2}$ and crosses a the major closed shell. Of particular interest for these systems is how the nuclear structure affects the isotope shifts and the atomic hyperfine structures.

From the experimental results compilation of Emrich et.al. /Emr.81/, systematics of radii and nuclear charge distributions were deduced from elastic electron scattering, muonic x-rays and optical isotope shift measurements. The differences in root mean square (rms) radii between isotopes showed systematic tendencies with a very distinct nuclear shell effect at magic numbers. One of the feature observed for many elements is that the differences in radii are largest at the beginning of a neutron shell and decrease linearly towards the end of the shell. Furthermore it was apparent that the isotope shifts were independent of the proton configuration of the nucleus involved ( e.g. the $^{86}Kr$ - $^{84}Kr$ and $^{88}Sr$ - $^{86}Sr$ isotope shifts were identical within the experimental uncertainties).

Lister et.al. /Lis.82/ studied the neutron deficient strontium isotopes $^{77-80}Sr$ with the gamma ray coincidence technique. These nuclei were observed to have electromagnetic properties with extremely large prolate deformation which were close to that of an ellipsoid with an axis ratio 3:2. The recent detailed study of Heyde et.al. /Hey.84/ of very neutron deficient nuclei with Z = 38,40 (Sr,Zr) has shown that, in regions near closed shells, indication for large quadrupole deformation connected with particular intruder orbitals existed. They expected a smooth change from strongly deformed nuclei (N = 40) toward anharmonic vibrational like spectra near closed shell N = 50.

The optical IS in the isotopes $^{84,86,88}Sr$ were first measured by Hughes /Hug.57/. He found no significant difference between the 84-86 and 86-88 shifts and concluded that, for both pairs, the volume shifts were consistent with zero. Heilig /Hei.61/ repeated the measurements with interferometric techniques and, in addition, measured 88-90 shifts. Regardless of the uncertainties due to unadequate knowledge of the specific mass effects, it was apparent that the 84-86 and 86-88 shifts were much smaller in magnitude than the 88-90 shift. Bruch et.al./Bru.69/ has normalized these data by using the isotope shift measurements in muonic or electronic x-ray spectra. The nuclear volume shift and mass dependent shift were determined.

Doppler free optogalvanic /Lor.82/ and two photon spectroscopy /Lor.83, Bei.83/ have been used for isotope shift measurements in transitions of SrI and SrII. Eliel et.al./Eli.83/ and Grundevik et.al./Gru.83/ investigated the hfs and the IS of low lying states in SrI by laser atomic beam and laser radio frequency double resonance techniques. Bender et.al. /Ben.84/ have performed a parametrical study of IS based on a simplified model and determined IS in five transitions of low lying states of SrI. The changes in mean square nuclear charge radius for the isotope pairs 86-88,86-87 and 84-86 have been calculated.

The IS of the levels $5p^2\ ^1D_2$ , $^1S_0$ and $5sns\ ^1S_0$ (n=7,8) of natural strontium isotopes have been measured in two-photon transitions from the ground state by Aspect et.al. /Asp.84/. These levels occurred below the beginning of the Rydberg series and are known to exhibit very strong configuration mixing. The optical spectra of the alkali-earth atoms with two electrons outside closed subshells are much more complicated than expected. This can be ascribed to the fact that both outer electrons are rather loosely bound and, therefore, strongly affected by the correlation phenomenon. Buchinger et.al. /Buc.85/ have measured all stable isotopes and two radioisotopes (A=89,90) by using atomic beam laser spectroscopy. By comparing the experimental data with droplet model predictions and Hartree-Fock plus BCS calculations, they suggested that the changes in ms charge radii are due to changes in size, a change in predominantly dynamic deformation, and a change in the diffuseness of the nuclear charge distribution. Martin et.al. /Mar.86/ had measured isotope shifts of the line 460 nm with an extension of the unstable neutron deficient isotope $^{82}$Sr. Recently Eastham et.al. /Eas.86, Eas.87/ applied the collinear fluorescence spectroscopy on a fast beam of strontium ions (SrII) of $^{78-84}$Sr. The deduced values of changes in nuclear charge radii were discussed in terms of changes in the static and dynamic nuclear deformations.

In the present work, the isotope shift and the hyperfine structure associated with an atomic transition to the excited P state of SrI are measured with a laser spectroscopic method. The experimental results can give a quantitative interpretation of the changes in mean square nuclear charge radii and the deformation of nuclear shapes on both sides of the neutron shell closure N = 50. The nuclear magnetic dipole moments and electric quadrupole moments can be derived from the measured hyperfine structure of the odd A isotopes.

# 2. EXPERIMENT

## 2.1. Laser Induced Fluorescence

The optical spectroscopic investigations of the excited Sr atoms are carried out by irradiating atoms with a laser beam of a suitable wavelength. The fluorescence photons emitted when the excited electrons transit to a lower energy state, are then measured. The atomic transition sequence of the SrI line used are $5s^2\ {}^1S_0$ - $5s6p\ {}^1P_1$ at wavelength 293.2 nm for the laser light absorption and the subsequent fluorescence of a transition $5s6p\ {}^1P_1$ - $5s4d\ {}^1D_2$ at wavelength 716.7 nm is observed. The system with these electronic transitions is shown schematically in Fig. 2.1. It is an alkali-earth like spectrum with a $5s^2\ {}^1S_o$ ground state. The radiative lifetime of the $5s6p\ {}^1P_1$ state is 65±5 nsec /Jön.84/ which corresponds to a natural linewidth of 2.45±0.20 MHz. The reason of choosing these transitions is due to a better peak resolution because of its longer lifetime when compared to the resonance state of $5s5p\ {}^1P_1$ with $\tau = 5.12$ nsec /Hul.64/ corresponding to a natural linewidth of 31 MHz. To minimize the problem of light straying from the laser beam directly into detector, fluorescent photons with an energy differing from the incident laser are preferred.

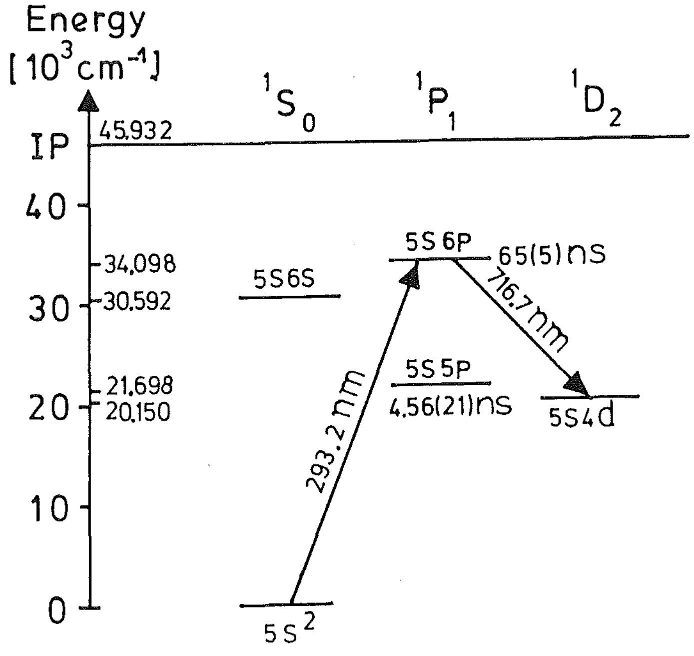

Fig. 2.1 The level scheme of electronic states of SrI. IP is the ionization potential energy of strontium atom.

## 2.2. Experimental Arrangement

The three major parts of the experimental apparatus are composed of: i) the laser system as a monochromatic light source ii) the atomizer apparatus to prepare an atomic beam of the sample and iii) the photon detection system with the data acquisition unit. A schematic diagram of the apparatus is shown in Fig.2.2.

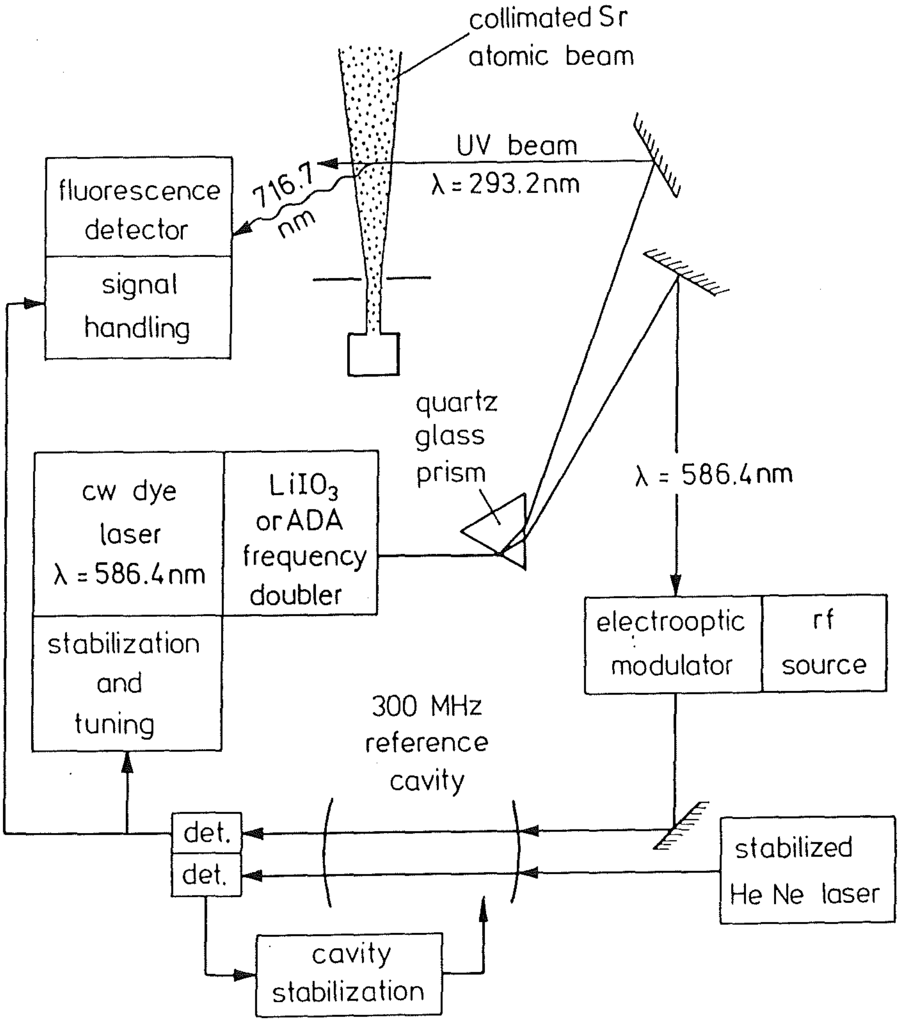

Fig. 2.2 Experimental arrangement for optical spectroscopy of strontium atoms

A high power argon laser is used as a light source for pumping a dye laser continuously. The tunable Rhodamine 6G ( R6G ) dye laser sent a laser beam of the wavelength 586.4 nm to a lens $L_1$ and was focused on a frequency doubler, an ammonium dihydrogen arsenate ( ADA ) or $LiIO_3$ crystal. The coherent cw ultraviolet light with a wavelength of 293.2 nm, which is the second harmonic , is then separated from a fundamental laser light by a dispersive quartz prism.

The uv beam is focused onto a well collimated strontium atomic beam at right angle for exciting atoms into the excited state. The interaction region is roughly cylindrical due to a small laser beam passing through a bundle of an atomic beam. Eventually the fluorescent light from the SrI line at 716.7 nm is collected by a large aperture aspheric lens and is then registered by the photomultiplier tube.

The dye laser is typically scanned with a frequency range of about 2 GHz, which covers most of the hfs range of the 293.2 nm strontium line. By this way, the spectrum of the atomic fluorescence intensity versus the frequency is obtained and is displayed on the multichannel analyser oscilloscope. Natural strontium metal of about 1 mg is heated in a vacuum chamber ( $10^{-5}$ mbar ) in a second reference oven and its atomic beam is also interacted perpendicularly with the uv beam. From the observed spectrum that is shown on an oscilloscope, one can visually adjust the region of interest and the scanning range of the dye laser.

The fundamental wavelength of the dye laser is to be selected for SrI measurement at 586.4 nm. In order to set the dye laser into the wavelength of interest rapidly, it could be achieved in two steps. At first, irradiation of iodine molecules in a quartz cell with the fundamental dye laser and then observation of the absorption spectrum. By comparing with the standard spectrum data which have been tabulated by Gerstenkorn and Luc /Ger.78/, one can find the actual wavelength region of the dye laser and can then tune to the wavelength of interest. The second step is to measure the dye laser wavelength with a wavemeter /Ste.84/. The single mode operation of the laser is checked by scanning the dye laser through two Fabry Perot interferometers (FPI) with free spectral ranges of 2 and 20 GHz. The major part of the fundamental laser is directed to a potassium dideuterium phosphate (KD*P) crystal modulator which is coupled with a radio frequency (rf) source and is further used for controlling the laser frequency stability by a method described in detail below. Some part of the fundamental laser is passed through a fixed 300 MHz reference etalon (FPI). The fringes are registered during strontium isotopes measurements and this is used as reference frequency markers.

Monitoring the uv intensity, the frequency doubler crystal is tuned to optimal second harmonic generation.

## 2.3. Laser System

### Argon Ion Laser and Tunable Ring Dye Laser

An argon ion laser (Coherent model CR-18 UV) is applied as a continuous wave (cw) source of high laser output power. Green light ( 514.5 nm ) with the peculiar characteristics of 1.9 mm beam diameter and a beam divergence of 0.43 mrad is used to optically pump dye molecules of a ring laser to the first excited band.

The tunable ring dye laser (Coherent model CR 699-21) utilizes an organic compound of Rhodamine 6 G ( R6G ) as an active medium. The outstanding qualities of a dye laser light beam are : i) the small beam divergence and the high linear polarization. ii) the large setting range iii) the high light intensity per phase space volume i.e. spectral width and the geometric quality. The dye R6G was dissolved in methanol ( 1.1g/50 ml) and then was mixed with a 1 litre of ethylene glycol as a solvent base. The lifetime of such a R6G solution for the operation is as long as about 1000 watt-hours.

At 8 watts pumping power the dye laser can provide 1.2 watt of single mode output power at the wavelength 586.4 nm. The dye laser beam diameter is 0.75 mm with the beam divergence of 1.6 mrad full angle. The effective tuning range of the cw dye laser with R6G is usually 560 to 650 nm with the maximum output power at 590 nm, which is thus optimum for a wavelength of 586.4 nm. The fine tuning of the dye laser frequency is performed by a Brewster plate or the laser resonator. The maximum continuous scan range is 30 GHz with 2% scan linearity.

### 2.4. Atomic Beam Apparatus

An atomic beam is a collision free stream of electrically neutral strontium atoms in a high vacuum system, while apertures shape its cross section as shown in Fig.2.3. The slit is used to reduce the Doppler width which occurs when a laser beam is crossed perpendicularly with the bundle of an atomic beam. The laser wavelength is tuned across an atomic absorption line. The Doppler width of the resulting absorption profile is reduced by a factor that depends on the collimation angle of the atomic beam. This is due to the fact that the thermal distribution of the atomic velocity component $v_z$ is reduced by the collimating apertures to $N(v_z) \alpha \exp( -mv_z^2 /\theta.2kT )$, where m is the mass of an atom , k is the Bolzmann constant, the angle $\theta = d/L$ , d is the slit width and L is the distance between the graphite diaphragm and the slit /Dem.80/.

The evaporation temperature of normal strontium metal in high vacuum of $10^{-5}$ mbar is around 600 °C. It requires an operating temperature upto 1400 °C to evaporate the enriched strontium isotopes, because the atoms of these samples were mass separated and implanted deeply into the surface of tantalum crucibles.

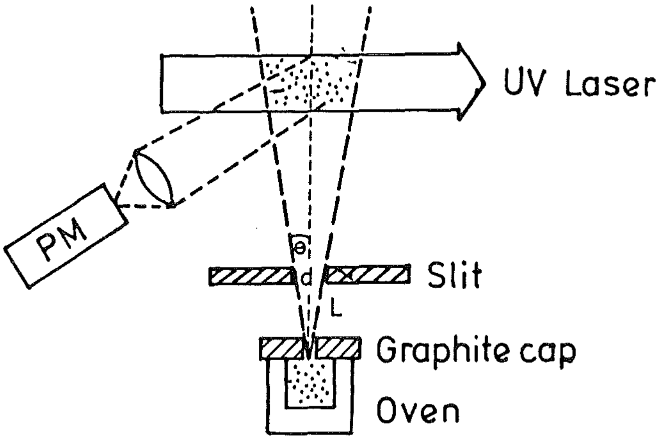

Fig. 2.3 Reduction of the Doppler width in a collimated atomic beam

**An electron bombardment oven comprising a tungsten filament of diameter 0.5 mm as a cathode was constructed. Although tungsten has a rather high work function (4.5 eV) it nevertheless has a very high melting point of 3380 °C which makes it suitable for long term operation. The tungsten filament is looped around the graphite anode and a current of about 30 A flows through this filament. The graphite anode is bombarded with electrons due to a high voltage of 2 kV applied to the cathode. An electric current of about 300 mA is sufficient to maintain the temperature of the graphite anode at 1400 °C. The anode temperature is measured by a thermocouple (Pt/Pt.Rh) which is embedded in the anode. The relation between the electric current and the temparature at the graphite anode is shown in the graph of Fig. 2.5.**

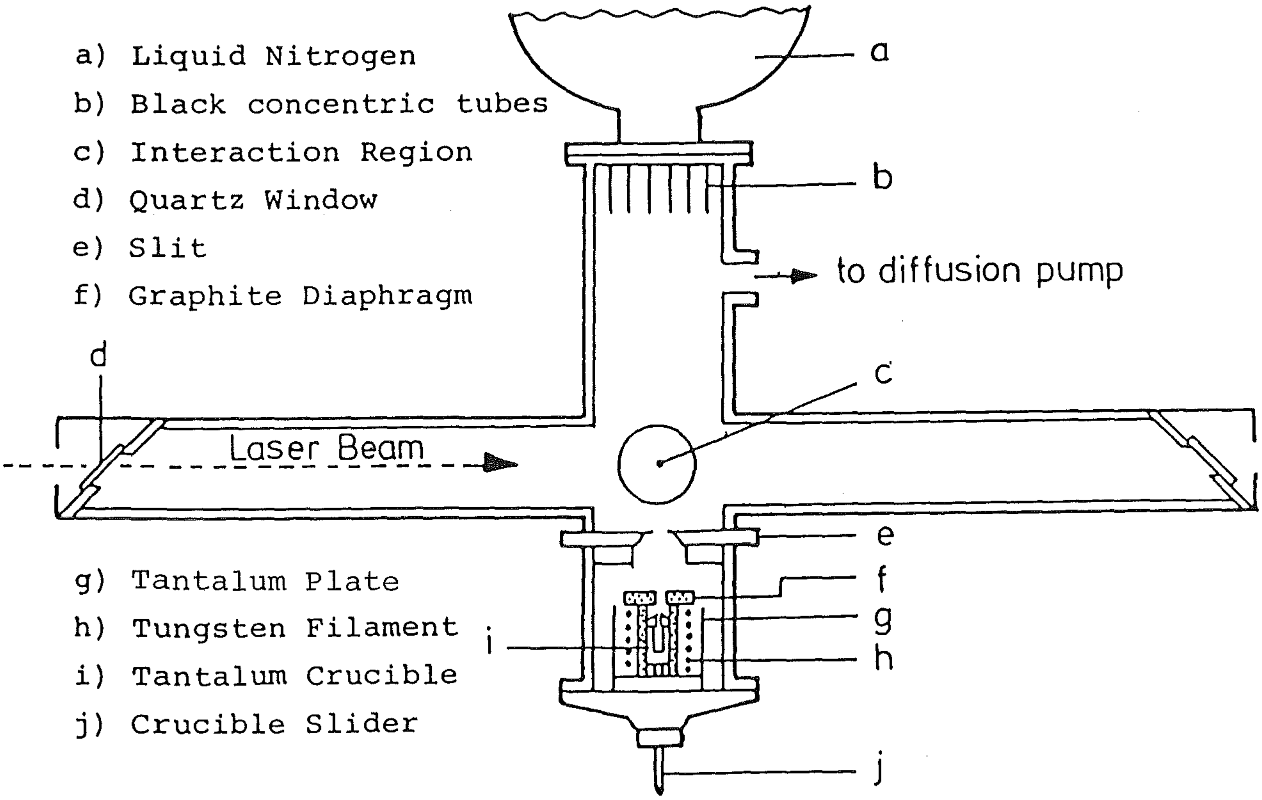

**<u>Fig. 2.4</u> Cross section of the atomic beam apparatus**

The high voltage of 2 kV accelerates the electrons from cathode filament to the anode. To keep constant this electron flow rate, the high voltage supply should be stable. The burst of some dust which has low boiling point or abrupt changes of the pressure in the vacuum chamber cause a changing rate of electron flow, which in turn effects the high voltage stability. It is therefore necessary to use an emission regulator to stabilize the electron bombardment current and a constant current power supply to generate the atomic beam.

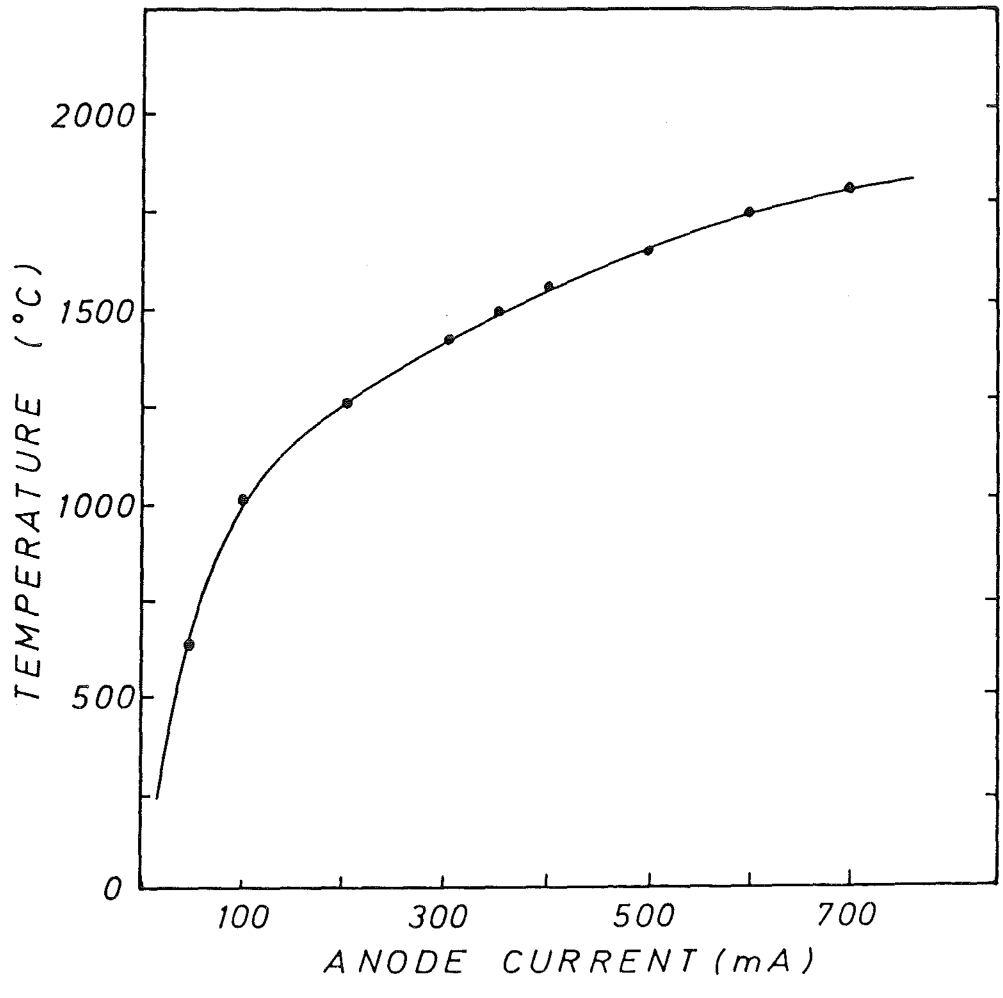

**Fig. 2.5** The relation between the electric current and the temperature at the graphite anode

## 2.5. Photon Counting System

Two models of the photomultiplier were selected to detect the fluorescent photons. A photomulplier RCA model C 31034-A02 with a gallium arsenide chip as a photocathode and with an in-line copper-beryllium dynode structure is appropriate for this measurement because of its high cathode response of about 12% quantum efficiency at 716.7 nm. The dark pulse rate is 12 counts per second (cps) at temperature –20 °C. In our cooling system using ethanol as a heat carrier, the housing temperature of the photomultiplier can be lowered down to –50 °C and the dark pulse rate is reduced to 0.3 cps when operated at 2.2 kV anode to cathode voltage. After the RCA photomultiplier was defected, the HAMAMATSU model R943-02 which has the same characteristics was applied. The photomultiplier is placed 0.55 m far from the interaction region to avoid any signal which occurs from gamma radiation of radioactive samples. It is shielded with lead bricks in order to reduce such a background.

The optical system used to observe the fluorescent light is shown in Fig.2.6. It is composed of a spherical mirror to reflect the light backward to the direction of the photomultiplier in order to gain more fluorescent signals. A condensor lens is used to focus all the light towards the cathode of the photomultiplier. An interference filter coupled with a blocking filter which is centered at the desired wavelength, filters all the light, but the 716.7 nm light can pass through. A quartz box is placed in front of the photomultiplier to prevent humidity at the surface window of the photomultiplier. An interference filter ( Schott type A3-0.3/ $\lambda$ = 716.4 nm) with 80.5 % transmission and 3.5 nm full width at half maximum ( FWHM ) is used to block the other wavelengths of light which originate from thermal radiation of the heated oven and some fluorescence light from other atomic transitions. The background count rate of the overall thermal radiation is 50 cps which could increase to 1500 cps when an empty tantalum crucible is inserted into the oven at temperature of about 1450 °C.

The signals from the photomultiplier were recorded and displayed on a Nuclear Data (ND-66) multichannel analyser. The photons were counted by means of the photomultiplier whose output fed a data acquisition system consisting of a Data General NOVA-3 minicomputer and its associated CAMAC modules.

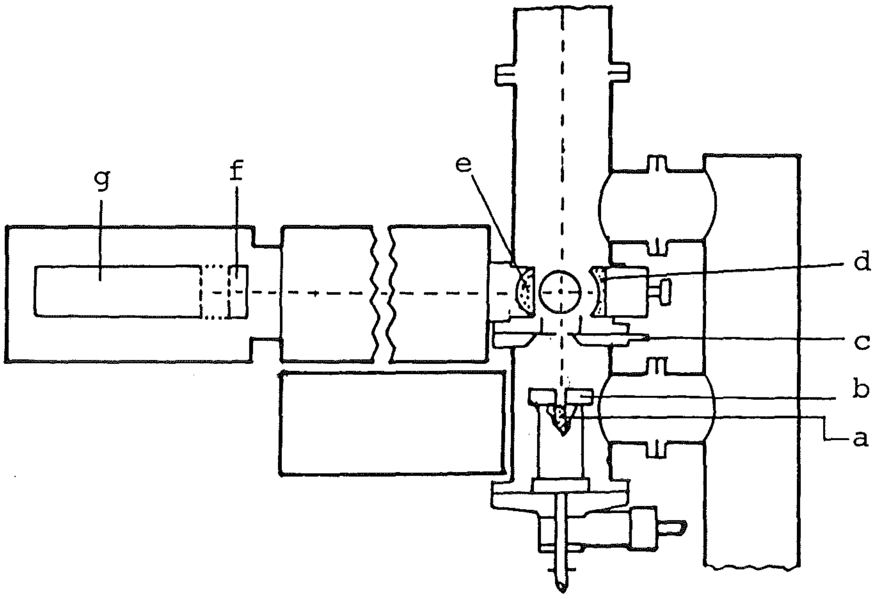

a) Oven Cartridge
b) Graphite Diaphragm
c) Slit (adjustable)
d) Spherical Mirror
e) Condensor Lens
f) Interference Filter
g) Photomultiplier

**Fig. 2.6** **Optical apparatus for measuring the emitted 716.7 nm photons. Centre of the circle is the interaction region between laser and strontium atoms.**

## 2.6. Methods of Measurement

The optical isotope shift in atomic spectra is of order MHz to GHz, very small when compared to the visible light of $10^{14}$ Hz. Such a small shift should be measured properly by laser spectroscopic techniques with a very high precision.

Instead of measuring the absolute emitted photon energies, the observed peak positions relative to some peak of reference were measured for the sake of accuracy. For Sr isotope measurements, the peak position of the neutron magic number isotope $^{88}$Sr (N=50) is used as a reference position. The distances of the other peaks far from the reference position are usually measured in units of frequency, either in megahertz ( MHz ) or in gigahertz ( GHz ). By this way, the isotope shifts and the hyperfine splitting components are obtained relatively in frequency units with the accuracy depending on the overall stability of the measuring unit.

Two methods of measurement are applied. Firstly, a multichannelscaling analysis (MCS) is a global and rough method. The cw laser was scanned internally with a long frequency range of about 3 GHz. All the resonant peaks of the hfs components could be observed in the spectrum. A rough value of the peak positions relative to the reference peak with an error of about 5 MHz could be obtained. The second method, the side-band measurement, is the finer method, in which the laser frequency stabilization by rf amplitude modulation to generate side frequencies is used to tune the cw dye laser with rf accuracy. By this method, accurrate values of about 200 kHz were obtained.

### 2.6.1. The Method of Multichannelscaling

A multichannel analyser (Nuclear Data Model ND-66) in multiscaling mode with an acquisition interface was used for starting and stopping a MCS sweep and for incrementing the counts in each channel. The MCS swept synchronously with the laser scan. An autosequence routine of operation which can be automatically repeated, was employed. The photon counts as a function of laser frequency were accumulated and recorded on a magnetic tape. The measuring conditions for MCS were previously selected with one millisecond dwell time per channel and ten sweeps over 1024 channels. The starting time was synchronized to the ring dye laser with an internal scan mode. Sweeping over the whole range frequency of about 3 GHz was sufficient to cover the total range of the strontium hyperfine structure components.

The great advantage of this MCS method is to search positions of the new isotopes that had never been measured. About 100 pg of the strontium isotopes were required for this measurement. A small amount of $^{88}$Sr (1ng) was added and used as a reference isotope. Due to the nonlinearity of the scanned laser frequency with the time, the frequency axis must be calibrated before and after the sample measurement by scanning the laser onto a 300 MHz Fabry Perot interferometer. The positions of the transmission fringes were recorded and then the frequency scale was interpolated for the calibration purpose. The cw laser was scanned repetitively by the internal scan mode and the data were stored on magnetic tape.

The total error of this method is about ±5 MHz which was partly due to the Doppler effect, because the collimating slit was opened for small samples to gain on peak signal to background ratio. The error was also generated by the frequency calibration due to the nonlinearity of the laser frequencies.

### 2.6.2. The Side-Band Method

In order to achieve a high precision of the frequency measurements, the laser frequency must be stabilized for a long term to reduce the frequency jitter /Bur.79/. This was achieved by locking it to a stabilized optical reference resonator, resulting in a fixed frequency laser system. In the side-band method an amplitude modulation of the dye laser beam with some radio frequency $\nu_{rf}$ by an electrooptic modulator ( Lasermetrics model 1080 ) was applied. The spectrum of the modulated light contains an unmodulated (carrier) frequency $\nu_{dye}$ as well as the sideband frequencies ( $\nu_{dye} + \nu_{rf}$ ) and ( $\nu_{dye} - \nu_{rf}$ ). These side frequencies can be used to achieve laser tuning.

In this set-up as shown in Fig. 2.7 /Ans.83/ one of the side bands is locked to the reference resonator (300 MHz.FSR) stabilized by an HeNe laser. The sideband lock is accomplished by a feed-back to the dye laser, i.e. the laser frequency is controlled such that the sideband chosen is held on the optical resonator peak. If the modulating frequency is altered, the laser frequency changes in such a way that the selected sideband frequency remains constant since it is locked to the fixed reference etalon; in other words, a fixed side frequency with changing modulation frequency change $\nu_{rf}$ leads to laser frequency change by exactly the same amount, thus rf-tuning of the dye laser frequency is achieved.

The rf synthesizer is operated under computer control; the laser is tuned in discrete steps of 5 or 10 MHz width across the resonance to be recorded. To speed up tuning and to reduce residual errors the computer generates an analog feed-forward voltage that closely matches the expected control signal. In this way a tuning range of 1 GHz is accessible which is only limited by the synthesizer and rf power amplifier available. Since the dye laser light is frequency doubled, the corresponding tuning range of the UV or atomic frequency in this experiment is 2 GHz. The tuning range can be further doubled by locking the high or low frequency sideband to the reference resonator in turn.

Since altogether three optical frequencies are present in the modulated beam, it is necessary to ensure that the proper sideband is brought in coincidence with a transmission peak of the reference etalon and is then selected to lock the laser. For this purpose a new feature was introduced, namely a frequency modulation of $\nu_{rf}$ with speed $\nu_{fm}$ and width $\Delta\nu$. Thus only the sidebands but not the carrier are frequency modulated. Locking a sideband frequency to the peak of the reference etalon is accomplished by phase sensitive detection at $\nu_{fm}$ with a lock-in amplifier. Both sidebands can be distinguished from each other by their relative modulation phase difference of 180°. Thus one sideband is identified by the choice of the lock-in-phase. Switching from one sideband to the other is then simply performed by inverting the phase-sensitive detector response.

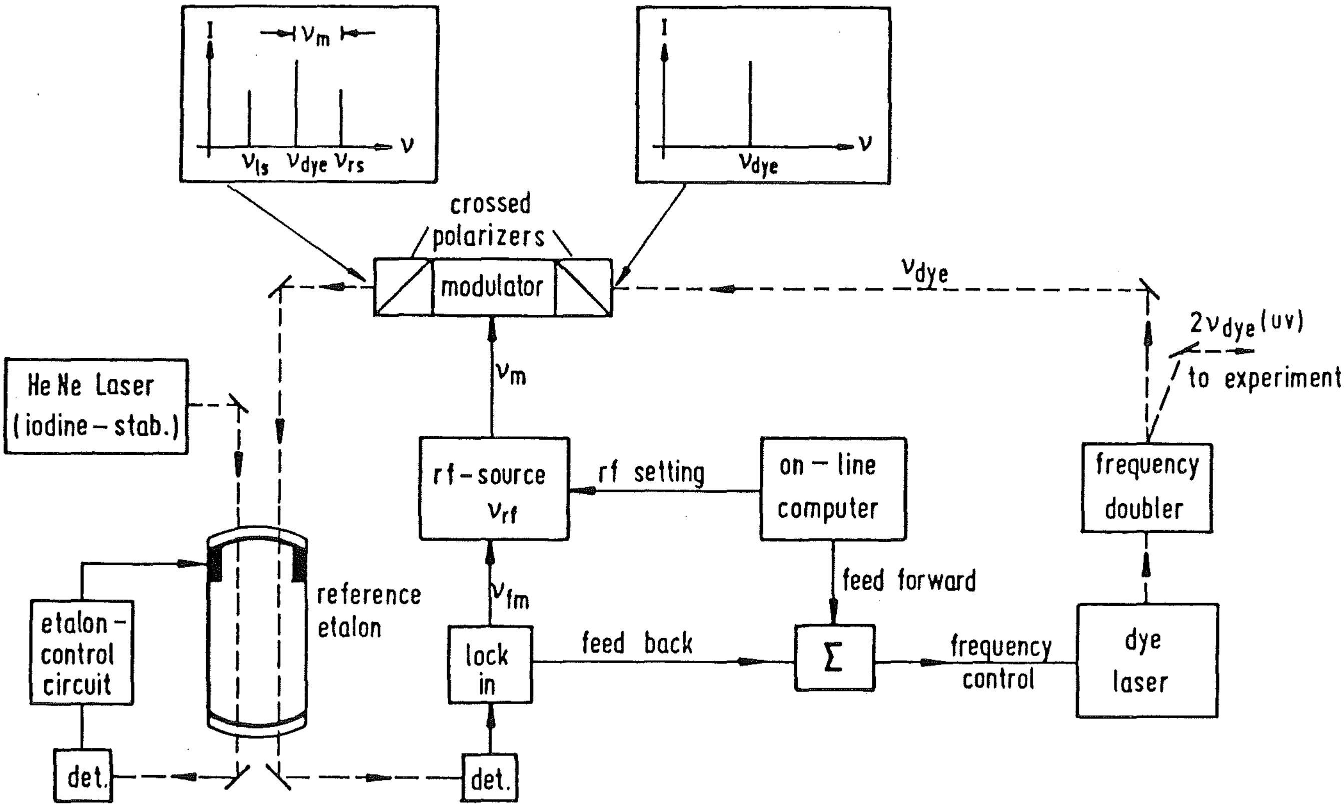

**Fig. 2.7** Schematic diagram of the laser side-band tuning system. The small graphs at the top show the frequency spectrum of the laser light before (right) and after (left) passing through the amplitude modulating unit.

## 2.7. Sample Preparation

The four stable isotopes of strontium as shown in Fig.2.8 are composed of one odd isotope with mass number A = 87 and three even isotopes with A = 84,86 and 88. The $^{88}$Sr is the neutron magic number isotope (N=50) and has the highest abundance of 82,58 %. The radioactive isotopes of strontium were produced by nuclear reactions. A long half-life $^{85}$Sr nuclide ($t_{1/2} = 65.2$ d) and the neutron rich isotopes ( A = 89 and 90 ) were purchased as nitrate solutions from Amersham and Buchler, Braunschweig, West Germany.

The neutron deficient isotopes $^{80,81,82,83,85m}$Sr were produced via an alpha irradiation of krypton gas at the isochronous cyclotron laboratory of the Karlsruhe Nuclear Research Center. The great advantages of the radioactive strontium production by this method are the high production cross section of these reactions, a large variety of the stable krypton isotopes and the rapid separation of the produced solid strontium from the gas target material. Krypton has six stable isotopes available as target material. Enriched krypton isotopes are used in order to yield larger amounts of the interesting strontium isotopes. Unfortunately the lighter isotopes such as $^{78}$Sr with half life 2.5±0.3 minutes /Lia.82/ and $^{79}$Sr with half life 2.30±0.10 minutes /Lis.79/ are not favorable for this experiment due to their short half lives.

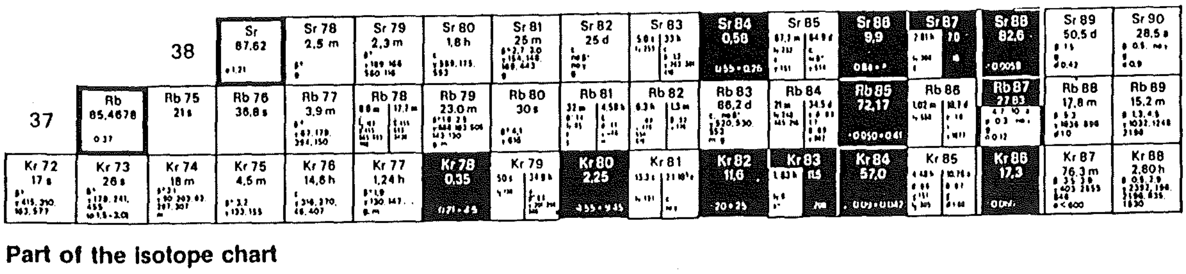

Fig. 2.8 Part of nuclide chart from Krypton (Z = 36) to Strontium (Z = 38)

**Fig.2.9 shows the cross section of the strontium isotope production apparatus /Feu.78, Bek.79/. The krypton gas from the stock vessel is filled into a tantalum tube ( 30 mm long and 5.5 mm inner diameter ) at a pressure of about 45 bar. The cyclotron alpha beam of energy 104 MeV is passed through a 5 mm diameter slit and a thin beryllium sheet in order to select the optimum alpha energy required for the nuclear reaction. The beryllium foils (f) of 10 $\mu$m thickness are of the double window type and used to maintain the krypton gas in the tube cavity (a). An indium foil is wrapped around the outer wall of the tube and contacted with the copper block which is used as a heat carrier. The tantalum tube is cooled by cold water (g) as well as by using compressed air (h). Strontium isotopes produced via $(\alpha,xn)$ reactions are deposited on the inner wall of the tantalum tube. After end of irradiation the krypton gas is pumped back by cooling the gas stock vessel with liquid nitrogen for a few minutes. The krypton gas is condensed and deposited on the wall. After this, the tantalum tube is transferred to an electromagnetic mass separator as an ionizer.**

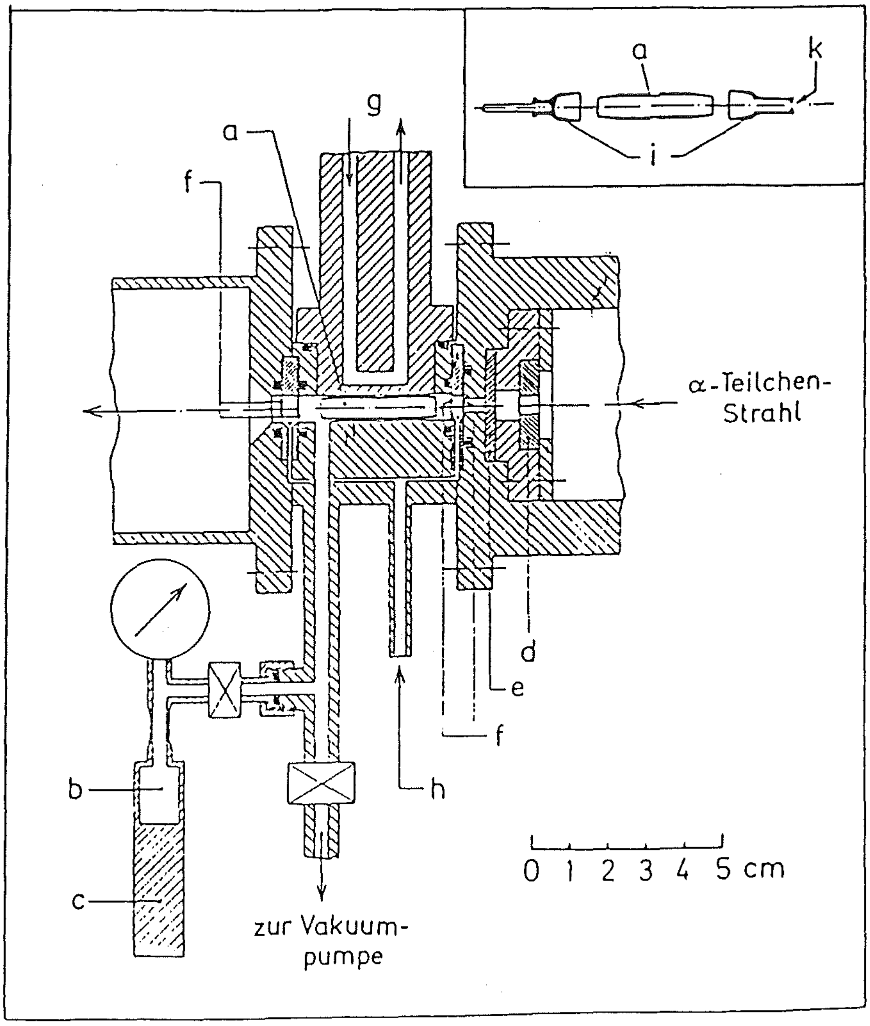

**Fig. 2. 9 Cross section of the radioactive strontium isotope production apparatus**

The isomers $^{85m}$Sr and $^{87m}$Sr have a low nuclear spin 1/2 in contrast to the considerably higher spin 9/2 of their respective ground states. Therefore the high angular momentum transfer in the ($\alpha$,xn) reaction leads to a very low isomer to ground state production ratio. For this reason a different production method had been applied. It is based on the fact that the unstable nucleus $^{87}$Y also has the nuclear spin 1/2 so that it decays exclusively into $^{87m}$Sr. The 82.2 hours half-life of $^{87}$Y is long enough to perform standard chemical separations. Because its lifetime is much longer than that of $^{87m}$Sr, a so-called radionuclide generator can be made. The procedure was as follows: rubidium chloride was bombarded with $\alpha$ particles to produce $^{87}$Y. The yttrium was separated from the target material and loaded into an ion exchange column. The decaying $^{87}$Y produced $^{87m}$Sr which was accumulated for several hours and then selectively washed out in amounts sufficient for a measurement.

The samples normally were purified by an electromagnetic mass separator /Fab.65, Fab.66/ that extracted the isotope of interest. In addition it ensured that the strontium was in elementary form. The procedure, however, could not be performed for $^{80,81,85m,87m}$Sr because of the 80 % losses in the separator. In these cases careful discrimination was required against impurities of other Sr isotopes produced along with that one under investigation. Quantitative gamma ray spectroscopy of the samples was useful in this situation to determine the sample composition.

If Sr in dissolved compound form was used (as for $^{85,89,90,87m}$Sr), a small amount of the solution was placed into the crucible and dried. When it was heated in the tantalum crucible, a sufficient portion of the Sr was evaporated in elementary form.

The minimum amount of the strontium isotope required for a sufficiently strong signal was about 60 pg or $4.10^{11}$ atoms. Most runs were performed with an amount of 100 to 800 pg as shown in the last column of Table 2.1. The first weight number refers to the amount used for the multiscaling method and the second weight number is for the method of side band measurement.

Table 2.1 Nuclear characteristics and nuclear reactions for the production of radioactive strontium

| A | N | b<br>(%) | I | $t_{1/2}$ | Nuclear Reaction | Weight (pg) |
|---|---|---|---|---|---|---|
| 80 | 42 | - | 0 | 1.8 h | $^{80}Kr(\alpha,4n)^{80}Sr$ | 100 |
| 81 | 43 | - | 1/2 | 22.2 m | $^{80}Kr(\alpha,3n)^{81}Sr$ | 100 |
| 82 | 44 | - | 0 | 25.5 d | $^{82}Kr(\alpha,4n)^{82}Sr$ | 200/600 |
| 83 | 45 | - | 7/2 | 32.4 h | $^{82}Kr(\alpha,3n)^{83}Sr$ | 400/820 |
| 84 | 46 | 0.56 | 0 | - | - | 100/500 |
| 85 | 47 | - | 9/2 | 64.9 d | $^{84}Kr(\alpha,3n)^{85}Sr$ | 200/1500 |
| 85m | 47 | - | 1/2 | 67.7 m | $^{84}Kr(\alpha,3n)^{85}Sr$ | 100 |
| 86 | 48 | 9.86 | 0 | - | - | 100/1000 |
| 87 | 49 | 7.00 | 9/2 | - | - | 100/1500 |
| 87m | 49 | - | 1/2 | 2.81 h | $^{85}Rb(\alpha,2n)^{87}Y$ | 60 |
| 88 | 50 | 82.58 | 0 | - | - | 100/1000 |
| 89 | 51 | - | 5/2 | 50.5 d | $^{88}Sr(n,\gamma)^{89}Sr$ | 230/500 |
| 90 | 52 | - | 0 | 28.5 a | fission | 100/860 |

# 3. UV PRODUCTION

It is of interest to study the electronic transition of the neutral atoms of strontium (SrI), $5s^2\ {}^1S_o$ – $5s6p\ {}^1P_1$ at 293.2 nm wavelength as described in 2.1. This wavelength is in the ultraviolet region. There are no stable dyes to produce any wavelength shorter than 330 nm and no accessible pump source to pump a cw uv dye laser. This monochromatic uv radiation is usually obtained by the interaction of the laser radiation with an appropriate nonlinear medium. The nonlinear optical device concept of a useful frequency doubler relies on the properties of an anisotropic crystal. The crystal should be birefringent with a high nonlinear susceptibility. An obvious requirement is that the crystal should be transparent for all frequencies and must have an excellent optical properties.

The propagation of electromagnetic (em) radiation through a nonlinear dielectric media of certain classes of crystal is described in detail by A. Yariv /Yar.79/ and F. Zernike and J.E. Midwinter /Zer.73/. Two methods of producing such a uv radiation are: i) frequency doubling the output of cw laser operating in the visible region , which is called the Second Harmonic Generation (SHG) and ii) mixing the output of two cw laser sources as called the Sum Frequency Mixing (SFM) /Cou.81/. The mixing of radiation at frequencies $w_1$ and $w_2$ to produce a new frequency $w_3$ is given by $w_1 + w_2 = w_3$. It is possible if the phase matching condition $w_3n(w_3) = w_1n(w_1) + w_2n(w_2)$ is satisfied. The $n(w_i)$ refers to the refractive index of the nonlinear medium for frequency $w_i$. In the case of SHG, this condition reduces to $n(w) = n(2w)$, as the same two input frequencies are used ($w_1 = w_2$).

The second harmonic power ($P_{2W}$) generated by a by a single mode, Gaussian beam of an angular frequency w and a power $P_W$ incident along the principal axis of a plane parallel slab of length L of a nonlinear crystal can be calculated by using the theory developed by G.D. Boyd and D.A. Kleinman /Boy.68/, which is given in MKS unit by

$$P_{2W} = \frac{JP_W^2 L^2 d^2 \sin^2 \Psi}{W_o} \cdot [\frac{\sin(\Delta KL/2)}{\Delta KL/2}]^2 \tag{3.1}$$

where J is the crystal dielectric constant at the fundamental frequency w. d is the coefficient of second harmonic generation determined by the material's nonlinear susceptibility. $W_o$ is the minimum beam radius and $\Psi$ is the angle between the crystal optic axis and the fundamental beam under phase matching conditions. $\Delta KL$ is a phase mismatch between the fundamental and the second harmonic beams.

## 3.1. Second Harmonic Generation by an ADA Crystal

A schematic of the experimental setup for laser system and uv generation is shown in Fig.3.1. An argon ion laser ($Ar^+$) which operates at a green line 514 nm with a 8 watts power, is used to pump a Coherent 699-21 ring dye laser. The ring dye laser operated with the dye Rhodamine 6G (R6G) at the 586.4 nm line gives a single axial mode output power of 1 watt to produce a 293.2 nm beam when applying an ammonium dihydrogen arsenate (ADA) crystal for the SHG process.

For the SHG, the ADA was used in type II 90° noncritical phase matching. The ADA crystal was chosen as a doubling crystal because of its optimum conversion coefficient for the SHG of dye R6G as observed by Blit et.al./Bli.78/. The ADA crystal has the conversion efficiency around $10^{-3}$ $W^{-1}$.

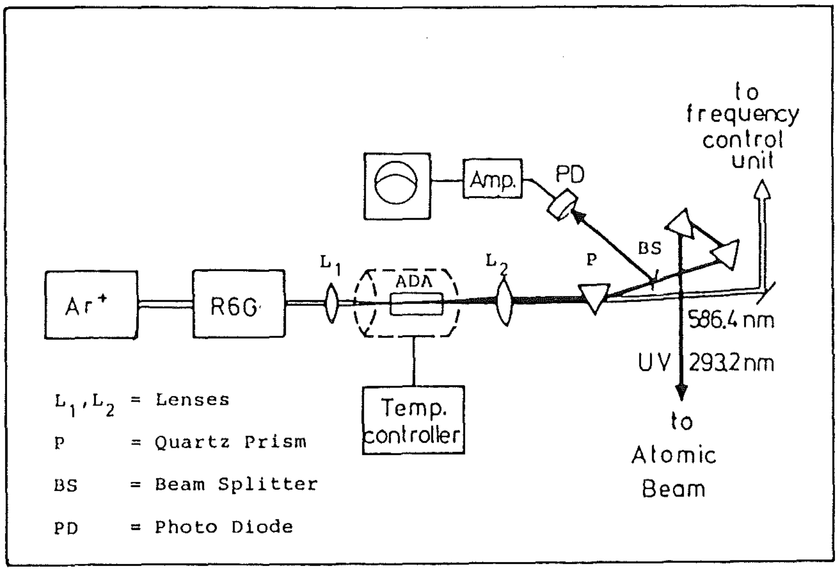

Fig. 3.1 Schematic diagram of the laser system used for producing single mode uv radiation around 293 nm by an ADA crystal.

From equation (3.1), the conversion coefficient C of the SHG process is equal to $P_{2w}/P_w$ and is inversely dependent on the beam waist radius ($W_o$) which requires that the beam be focused onto the nonlinear crystal. In order to achieve the maximum power density of the fundamental radiation inside the ADA crystal, the beam of the dye laser is focused by the lens $L_1$ (F20mm) at the center of ADA crystal. The single domain ADA crystal has the dimensions axbxc = 50x8x8 mm, where a is the length along the direction of light propagation. To achieve SHG for the wavelength used, the ADA crystal must be maintained stable at a distinct temperature.

A Haake thermostat model F3-Q is employed for this purpose. An ethanol solution is cooled at a continuous operation and can reach to –70 °C. The temperature of the F3-device can be tuned between –65 to +50 °C. For cooling the ADA crystal, the ethanol is circulated from the thermostat into the metal housing of the ADA crystal. In this manner the ADA crystal temperature can be maintained stable to ±0.05 °C.

The temperature characteristics of the ADA crystal were determined by Marshall et.al./Mar.80/. Analysis of the temperature tuning data obtained for SHG in ADA showed that for any crystal temperature T (°C) in the range from –40 °C to 100 °C the corresponding fundamental wavelength (nm) is given to a good approximation (±0.2 nm) by

$$\lambda_m = 577.7 + \alpha T + \beta T^2 \tag{3.2}$$

where the empirical constants $\alpha = 0.281$ nm/°C and $\beta = 0.00055$ nm/(°C)$^2$. The wavelength can be temperature tuned at a rate $d\lambda/dT = 0.3$ nm/°C.

The fundamental wavelength of 586.4 nm required an operating temperature of 29.59 °C. The ADA crystal is positioned in a beam waist of the fundamental radiation from the front lens $L_1$. The beam waist radius was measured to about 15 $\mu$m. The generated uv radiation propagated through a second quartz lens $L_2$ (f160mm), which is transparent for uv and serves as a recollimating output lens. With the fundamental input power ($P_w$) of 1.2 watts at 586.4 nm, about 1.2 mW ($P_{2w}$) of second harmonic radiation is obtained. This corresponds to a conversion coefficient of $1 \times 10^{-3}$ $W^{-1}$ for this SHG process. The uv output power was measured with a calibrated thermopile ( Pyroelectric Radiation model Rk-5100 from Laser Precision Corp.). The 293.2 nm uv output power remains stable for some hours of operation. High laser power may induce additional losses due to thermal effects in the crystal but this can be neglected because the absorption coefficient of the crystal is lower than 0.1 %/cm /Frö.76/.

## 3.2. Second Harmonic Generation by $LiIO_3$ Crystal

In order to improve the sensitivity of the measurement, the uv light power should be increased. The method is based on an extracavity SHG using an angle tuned lithium iodate ($LiIO_3$) crystal.

The $LiIO_3$ single crystal of 5 mm thickness obtained from Gsänger Optische Komponenten is generated from aqueous solution and belongs to a space group $P6_3$. This crystal offers great advantages of mechanical stability over a wide temperature range (20–250 °C) and relative freedom from degradation in a normal room environment. This crystal is easily polished with diamond paste and without deterioration of the polished surface when the crystal is kept in dry air for a long time. Since the refractive indices are very stable with respect to the temperature /Nat.69/, the phase matching is achieved rapidly by an angle tuning. The tuning range for SHG of this crystal is limited to 292-315 nm. Its doubling characteristics has been studied in detail by Buesener et. al. /Bue.86/.

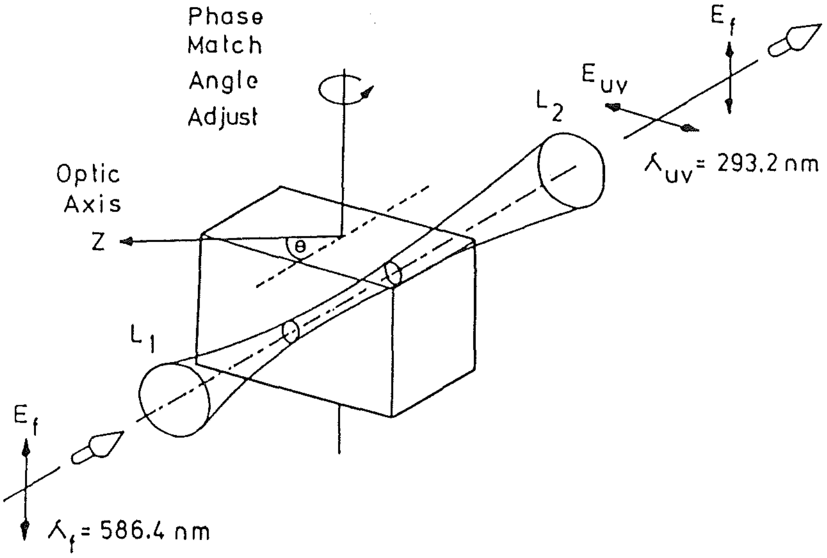

**Fig. 3.2** Geometry of the angle matched second harmonic generation for $LiIO_3$ crystal. $L_1$ and $L_2$ are thin lenses with focal lengths $f_1$ 20 mm and $f_2$ 100 mm.

In the optical arrangement as shown in Fig.3.2, the fundamental laser beam is focused by the lens $L_1$ and the bundle of the laser will expand until it reaches the second lens $L_2$. From lens $L_2$ lens, it will emerge as a bundle parallel to the axis again.

About 3 - 4 milliwatts of uv radiation at 293.2 nm was obtainable when using R6G dye laser at 1.2 watt. The SHG efficiency of the $LiIO_3$ crystal is 4 times greater than when using the ADA crystal at the same condition. When a high power laser is focused on this crystal, it is slowly degraded. The thermally induced losses in the crystal are of particular importance, which are caused by absorption of the laser radiation within the dielectric medium, creating a temperature profile across the laser beam. The absorption coefficient of the crystal is more than 10 %/cm /Nat.69/ due to an increasing phase mismatching in the crystal. To avoid the residual absorption of the laser which causes this thermal defocusing, a movable table was constructed in order to move the crystal in a horizontal direction perpendicular to the laser beam. The table is moved by a step motor with the speed of about 1 mm/min.

# 4. RESULTS

The induced transition of a valence electron from ground state to the second excited P state ( $5s^2\ {}^1S_0 - 5s6p\ {}^1P_1$, $\lambda = 293.2$ nm ) of SrI was achieved by laser excitation of the neutral strontium atoms. In decaying to the lower quantum state of $5s4d\ {}^1D_2$, the emitted photons of wavelength 716.7 nm were observed. A typical spectrum showing the positions of all four stable strontium isotopes ( 84:0.56%, 86:9.86%, 87:7.02%, 88:82.16% ) is given in Fig.4.1. The actual computer plot is shown where the data are distributed over 1024 channels correspoding to the frequency range of about 2 GHz. The odd isotope A = 87 shows three peaks due to the splitting of the hyperfine structure. The three even isotopes are shown by the equidistant peaks in a queue along the frequency axis, which represents the isotope shift effect.

The observed line width of 30 MHz at FWHM, is the mixture of the natural linewidth 2.5 MHz ( Chapter 2.1 ) and a dominant residual Doppler broadening due to the high oven temperature (>1200°C). The slit diameter allowing the bundle of atoms to pass through contributes to the Doppler effect. A good spectrum resolution can be seen from the clearly resolved peaks of A = 86 and one of A = 87 with 30 MHz distance. The peak intensities are directly proportional to the amount in weight of the corresponding isotopes.

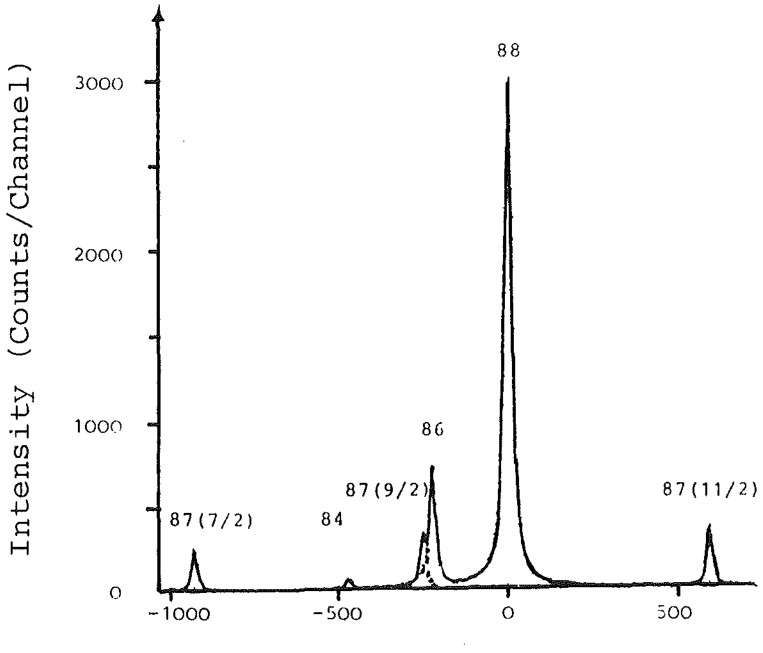

Fig. 4.1 Optical spectrum of SrI ($\lambda = 293.2$ nm) from the stable strontium isotopes

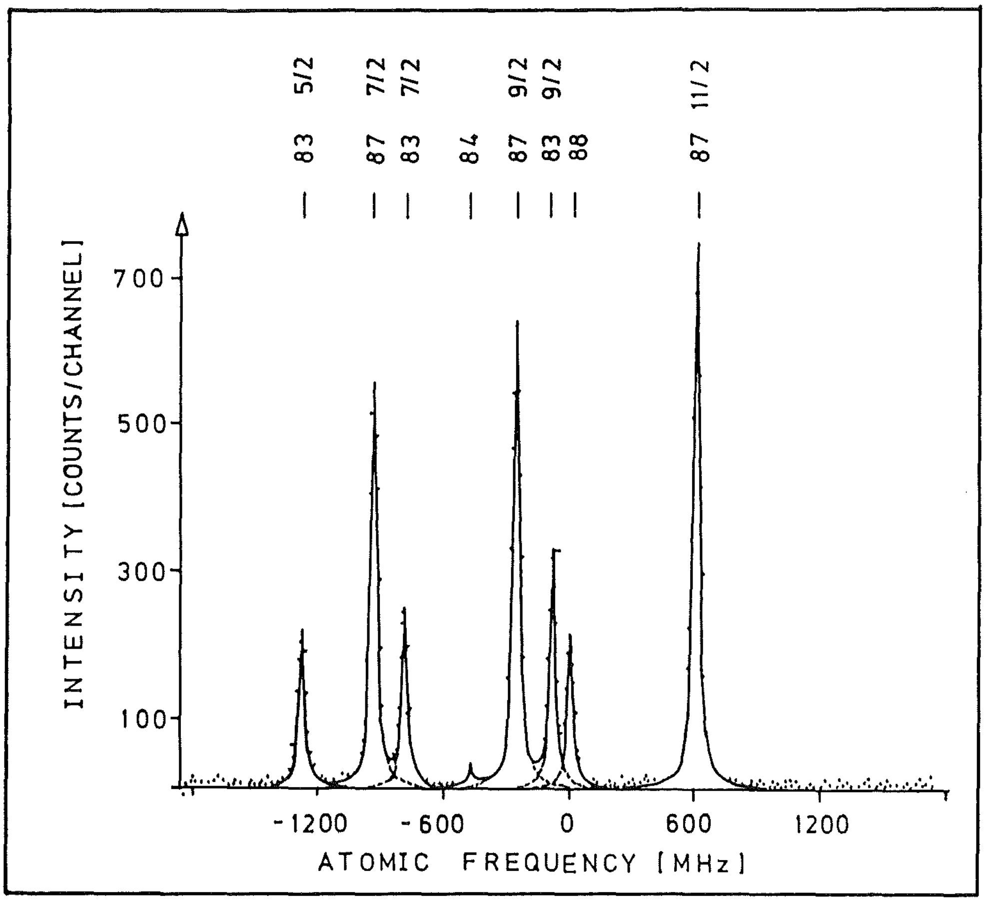

**Fig. 4.2** **The hyperfine splitting spectrum of odd A isotopes ( A=83 and 87). $^{88}$Sr and $^{84}$Sr occured as impurities in the crucible.**

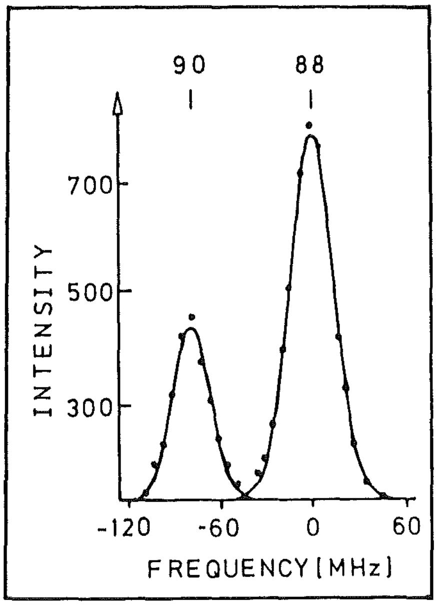

**Fig. 4.3** **The spectrum of $^{90}$Sr and $^{88}$Sr measured by the side-band method with 6 MHz per channel**

Fig.4.2 shows the fluorescence spectrum of two odd isotopes $^{83}$Sr and $^{87}$Sr which resulted in a splitting of the hfs components. The radioactive $^{83}$Sr ($t_{1/2}$ = 32.4 h ) was about 500 pg and 1 ng of the stable isotope $^{87}$Sr was added as a reference by an electromagnetic isotope separator. $^{88}$Sr and a small peak of $^{84}$Sr occured as impurities in the uncleaned tantalum crucible which remained from a previous experiments. The atomic frequency scale is counted from the reference peak position of $^{88}$Sr. The peak position of $^{90}$Sr relative to $^{88}$Sr as shown in Fig.4.3 is a typical spectrum measured by the side-band method. The laser frequency was changed by the computer controlled procedure and using 6 MHz per channel.

The results of peak positions which were observed by using the multiscaling (MCS) and the side-band (SB) methods are compiled in Table 4.1. The isotope shifts and hfs of the strontium isotopes between A = 80 to 90 including two isomeric nuclei 85m and 87m are determined across the major neutron closed shell (N=50, A=88). The experimental errors quoted are statistical and arise from the uncertainties in the determination of the positions of the calibration fringes from the reference FPI and the resonant isotope peaks. The statistical errors in the determination of frequency intervals are estimated from an analysis of several identical measurements, which are eventually averaged. Possible systematic errors may result from nonlinearities of the dye laser frequency scan. These nonlinearities are estimated from the dispersion of the measured free spectral range (FSR) of the reference 300 MHz FPI, when scanning the dye laser over a long frequency range. The uncertainty in the length of the reference cavity give rise to an additional error contribution. The long term frequency drift of the dye laser also accounts for random error. The sources of errors, both the statistical fluctuations and the estimated possible systematic errors were treated in more detail in /Ans.85/. The parameters that were varied to test their influence on the frequency difference determination are: laser intensity, direction of the atomic and light beams, atomic beam collimation, oven temperature changes and laser frequency control and tuning characteristics. The result showed that the uncertainty for the determination of natural strontium peak positions was typically 50 kHz. The other feature that limits the accuracy of the results is the observed linewidth of the resonances. The precision, which is an inherent portion of the linewidth, is about 1% of the experimental FWHM.

Table 4.1 Hyperfine component positions and isotope shifts for strontium isotopes and isomers for the optical transition = 293.2 nm. $^{88}$Sr was chosen as the reference for the frequencies.

| Mass Number A | Nuclear Spin I | Total Angular Momentum F | Component Position $\nu^{A} - \nu^{88}_{cm}$ (MHz) |
|---|---|---|---|
| 80 | 0 | 1 | -992(5) |
| 81 | 1/2 | 1/2 | -200(8) |
| | | 3/2 | -1221(5) |
| 82 | 0 | 1 | -728.4(5) |
| 83 | 7/2 | 5/2 | -1264.5(3) |
| | | 7/2 | -782.5(5) |
| | | 9/2 | -84.4(3) |
| 84 | 0 | 1 | -474.06(5) |
| 85 | 9/2 | 7/2 | -1077.7(2) |
| | | 9/2 | -462.8(2) |
| | | 11/2 | +317.2(3) |
| 85m | 1/2 | 1/2 | +414.5(3.0) |
| | | 3/2 | -715.4(1.5) |
| 86 | 0 | 1 | -224.73(5) |
| 87 | 9/2 | 7/2 | -927.85(10) |
| | | 9/2 | -254.95(10) |
| | | 11/2 | +596.97(10) |
| 87m | 1/2 | 1/2 | +905(15) |
| | | 3/2 | -580(10) |
| 88 | 0 | 1 | 0 |
| 89 | 5/2 | 3/2 | -1044.5(5) |
| | | 5/2 | -304.8(4) |
| | | 7/2 | +692.8(1.0) |
| 90 | 0 | 1 | -79.7(3) |

Considering the consistency of the experimental results, we relate our isotope shifts ($\lambda = 293.2$ nm) to those in the transition $5s^2\ ^1S_0 - 5s5p\ ^1P_1$ at $\lambda = 460.7$ nm transition from /Eli.83, Buc.85/ by the King plot method (see Chapter 5.1). The modified isotope shift quantity $(\nu^{88} - \nu^{A})\cdot 88\cdot A/(88-A)$ for the 293.2 nm line is plotted against the same expression for the 460.7 nm line as shown in Fig.4.4. /Ans.86/. The five points do not lie on a straight line in contradiction to the standard theory of the isotope shifts as suggested by Kuhn /Kuh.69/. Fig.4.4 also shows the possibilities of the King lines. The dotted area give the range of the King line due to the uncertainty of the results for the four stable isotopes ($^{84,86,87,88}$Sr) and its spread does not meet the $^{89,90}$Sr data points. From this discrepancy, it could be concluded that the $^{89,90}$Sr data must be in error / Ans.86 /.

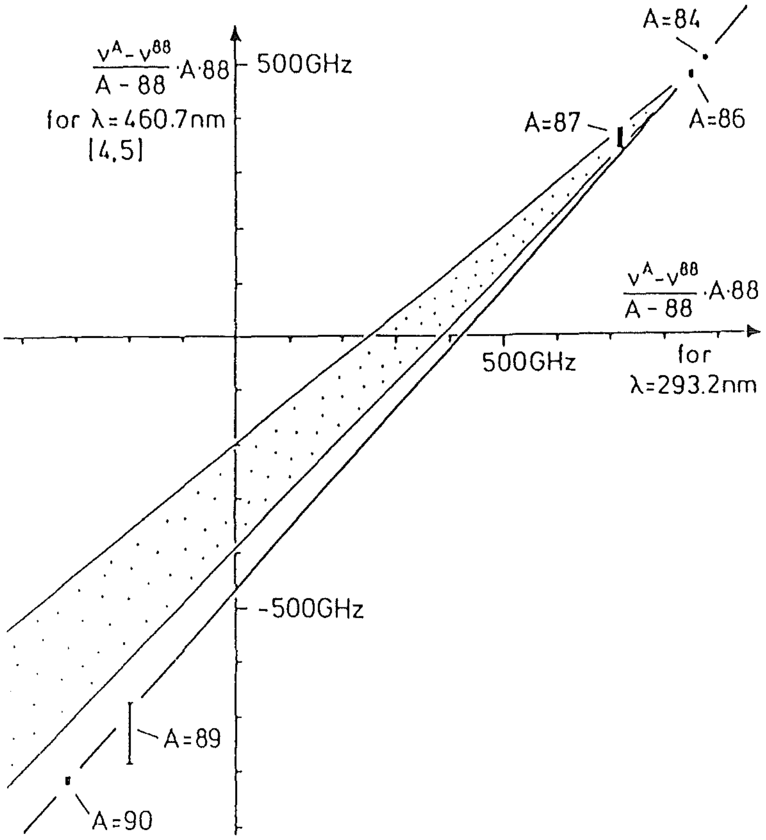

**Fig. 4.4** King plot of the modified IS between SrI (293.2 nm) line and the 470.6 nm line from /Buc.85/

# 5. INTERPRETATION

## 5.1. Isotope Shifts and Mean Square Charge Radii

The isotope shift (IS) is defined as a difference of the atomic transition energies between two isotopes. The effect can be seen clearly in Fig.4.1. This typical spectrum shows the peak positions of the even A isotopes (A = 84,86,88) in which the distances are: 224.73 MHz for $^{84-86}$Sr and 249.33 MHz for $^{86-88}$Sr. The isotope shift values obtained in this experiment are shown graphically in Fig.5.1. The values for the odd A isotopes are obtained from determining the centers of mass of the hfs levels.

For a given transition, the IS between two isotopes which the neutron numbers are changed with mass numbers A and A$'$ originates from two mechanisms. The first is due to a change of nuclear mass of the isotopes and is called the mass shift effect (MS) and the other part arises from changes of size and shape of the electronic charge distribution of the nuclei which is called the field shift (FS) or the volume shift effect.

Following the notations in many reviews concerning the theory of isotope shift /Sta.66, Hei.74, Bau.76, Sch.80, Kin.84/, the experimental isotope shift in an atomic transition i is expressed as follows:

$$IS = MS + FS \tag{5.1}$$

$$\Delta\nu_i^{AA'} = M_i \frac{A' - A}{AA'} + F_i \lambda^{AA'} \tag{5.2}$$

where $\Delta\nu_i^{AA'}$ is the frequency difference between two optical peaks of isotopes. $M_i$ and $F_i$ are the parameters for mass and field effects, respectively. $\lambda^{AA'}$ is a parameter carrying the information about changes of the nuclear charge distribution.

### 5.1.1. Mass Shift

The mass shift can be split into a normal mass shift (NMS) and a specific mass shift (SMS)

$$M_i = M_{i(NMS)} + M_{i(SMS)} \tag{5.3}$$

The normal mass shift is due to changes in the reduced mass and can be calculated as

$$\begin{aligned} M_{i(NMS)} &= \frac{m_e}{m_p} \cdot \nu_i \\ &= \frac{1}{1836.15} \cdot \nu_i \end{aligned} \tag{5.4}$$

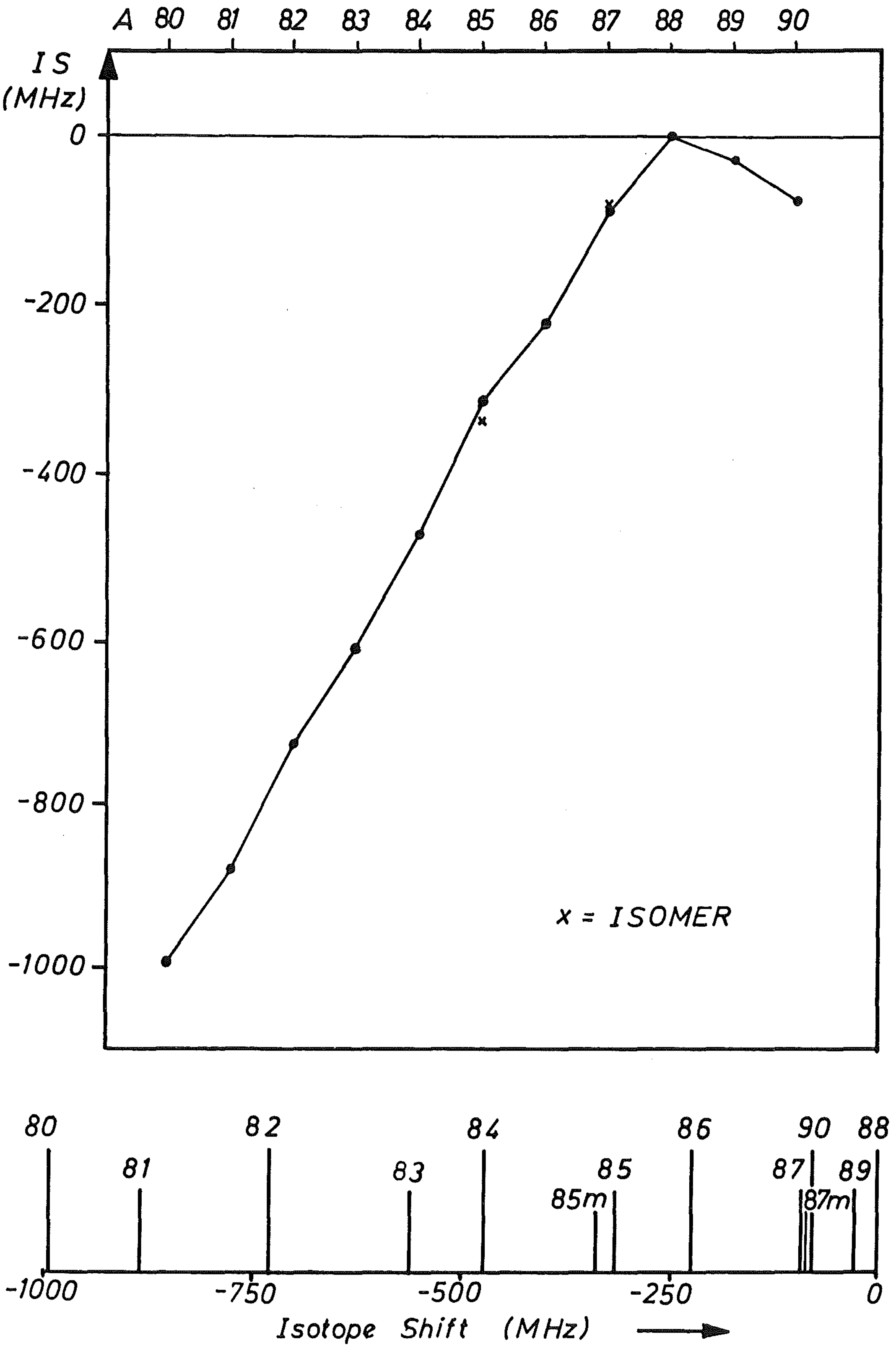

**Fig. 5.1** Isotope shifts of the transition $5s^2\ ^1S_0 - 5s6p\ ^1P_1$ ($\lambda = 293.2$ nm) of SrI relative to $^{88}$Sr. The experimental errors are smaller than the points.

where $m_e/m_p$ is the electron to proton mass ratio and $\nu_i$ is the transition frequency (in our case 293.2 nm = $1.02225\mathrm{x}10^{15}$ $s^{-1}$ and $M_{i(NMS)} = 5.569\mathrm{x}10^{11}$ $s^{-1}$).

The specific mass shift arises from the influence of correlations in the motion of the orbital electrons on the recoil energy of the nucleus as given by:

$$M_{i(SMS)} = \frac{1}{M} \sum_{k>j=1}^{n} \vec{P}_j \cdot \vec{P}_k \tag{5.5}$$

where $\vec{P}_j$ and $\vec{P}_k$ are electron momenta of the electron j and k, respectively. M is the nuclear mass and n is the number of electrons in atom. The factor $M_{i(SMS)}$ can be positive or negative depending on the correlation between all electrons and can be calculated so long as the wave function is known. Like the normal shift, the SMS falls off as $1/M^2$ with increasing M, and is very small in the heavy elements.

### 5.1.2. Field shift

The field shift effect originates from the variation of the finite size and the angular shape of the nuclear charge distribution when neutrons are added to the nucleus. Consequently the binding energy of s- electrons differs for different isotopes. The monopole term of the electrostatic energy for an electron in the field of the nuclear charge distribution is given by:

$$V_{e^-} = e \int \rho_e \phi_n d\tau \tag{5.6}$$

where $\rho_e$ is the electron density and $\phi_n$ is the nuclear potential. Consequently for an atomic transition:

$$\Delta V_{e^-} = e \int \Delta\rho_e \phi_n d\tau \tag{5.7}$$

where $\Delta\rho_e$ is the difference in electron densities between the atomic states, and the shift between isotopes A and A′ is given by:

$$\Delta V_{e^-}^{AA'} = e \int \Delta\rho_e \Delta\phi_n d\tau \tag{5.8}$$

where $\Delta\phi_n$ is potential difference between isotope A and A′. The parameter $F_i$ ( see eq.5.2 ) may be factorized as /Hei.74/

$$F_i = E_i \cdot f(Z) \cdot \beta \tag{5.9}$$

where the electronic factor $E_i$ depends on the change of the total nonrelativistic electronic charge density at the point nucleus, $\Delta\rho_e = \Delta|\Psi(r{=}0)|_i^2$ in the corresponding electronic transition i

$$E_i = \frac{\pi a_o^3}{Z}\Delta|\Psi(0)|_i^2 \tag{5.10}$$

where $a_o$ is the first Bohr radius and equal to $h^2/m_e c^2 = 5.29177\text{x}10^{-11}$ m and Z is the atomic number. $\beta$ is the screening effect and takes into account the change in the screening of inner closed shell electrons from the nuclear charge by the valence electron as it changes from ns to np states /Hei.74/.

The factor f(Z) is a function which increases with Z and accounts for the relativistic correction to $E_i$ and for the finite nuclear charge distribution. Adopting a uniformly charged sphere of the radius $R = r_o A^{1/3}$ the function f(z) has been evaluated by Babushkin /Bab.62, Bab.63, Fra.62/, slightly improved by Zimmermann /Zim.84/. Historically /Bri.52/ f(z) is expressed in terms of the " isotope shift constant ".

The nuclear parameter $\lambda^{AA'}$ can be expressed as a power series of the mean charge radii differences /Sel.69/,

$$\lambda^{AA'} = \delta < r^2 > + \frac{C_2}{C_1}\delta < r^4 > \frac{C_3}{C_1}\delta < r^6 > + \cdots \tag{5.11}$$

Since to a good approximation, the electron wave function can be considered constant over the nuclear volume, the contribution of the higher charge moments are very small /Hei.74/, usually smaller than the errors in the evaluation of $\lambda^{AA'}$ from the optical measurement; i.e.

$$\lambda^{AA'} \approx \delta < r^2 > \tag{5.12}$$

### 5.1.3. King Plot

The separation of the experimental isotope shifts into mass shift and field shift is usually performed by a King Plot procedure /Kin.63/. The relation of the IS between two atomic transitions i and j is shown in the following way:

$$\delta\nu^{AA'}_{i,RIS}\frac{AA'}{A-A'} = \delta\nu^{AA'}_{j,RIS}\frac{AA'}{A-A'}\frac{F_i}{F_j} + (M_{i,SMS} - M_{j,SMS}\frac{F_i}{F_j}) \qquad (5.13)$$

where $\delta\nu^{AA'}_{i,RIS}$ is the residual isotope shift of the transition i in which the NMS has been subtracted from the experimental IS. The King plot procedure is the plot between two modified isotope shifts for pairs of AA', where in general the points should fall on a straight line /Kuh.69/. The extracted quantities from the graph are the slopes $F_i/F_j$ and the intercepts $M_{i,SMS}$ - $M_{j,SMS}\cdot F_i/F_j$.

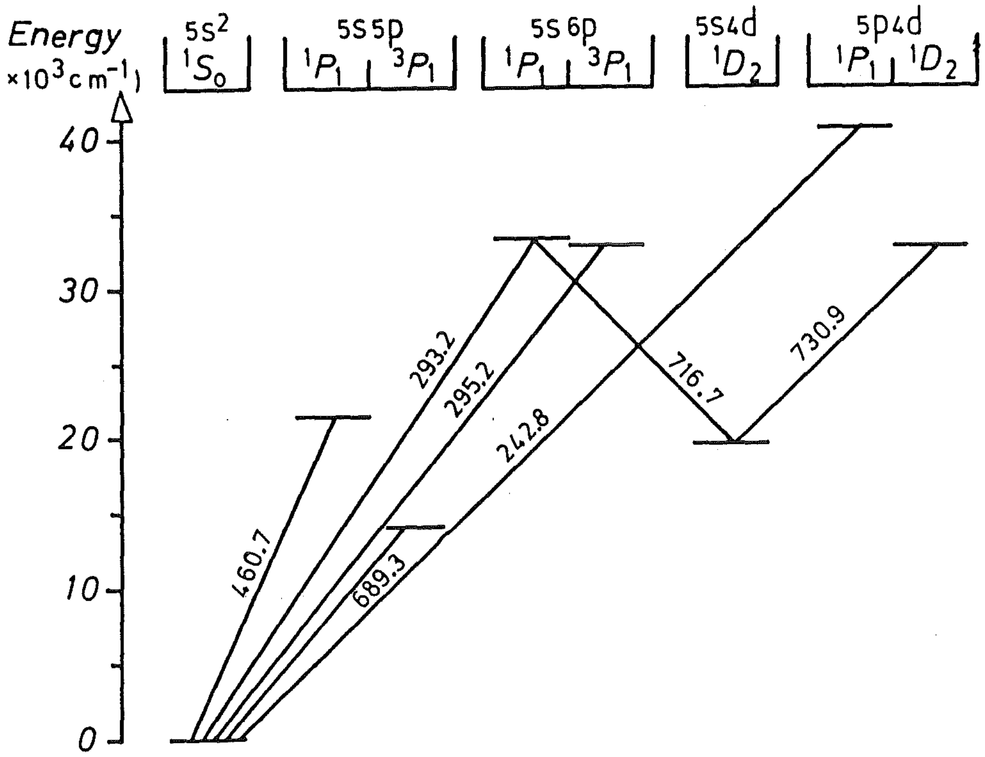

Fig.5.2 Energy level diagram of SrI with the observed transitions

The results of the isotope shift measurement for the 293.2 nm line in this experiment are presented in Table 5.1 with the previously studied other transition lines. The measured transition isotope shifts relative to A = 88 strontium are given in MHz. A negative sign in 716.7 nm line means that the lighter isotope is shifted toward a larger frequency. The observed atomic transitions for the neutral strontium atoms (SrI) are shown in Fig.5.2 with energy levels of the corresponding electronic states. The transition lines are labelled with the values of wavelength in nm. The ionic transition line of 421.6 nm (SrII) is not shown in this diagram. The experimental data are presented in Table 5.1.

Table 5.1 Observed transition isotope shifts relative to $^{88}$Sr ( in MHz ) of the strontium atoms

| Line (nm) | Transition | Isotope Shift $\nu^{88} - \nu^{A}$ (MHz) | | | | |
|---|---|---|---|---|---|---|
| | | 84 | 86 | 87 | 89 | 90 |
| 421.6[a] | $5s\ ^2S_{1/2} - 5p\ ^2P_{1/2}$ | 361(25) | 167(13) | 59(7) | | |
| 460.7[b] | $5s^2\ ^1S_o - 5s5p\ ^1P_1$ | 270.8(1.4) | 124.8(3) | 46.3(2.0) | | |
| c | | 270.6(2.4) | 124.5(1.3) | 49.2(3.6) | 93.1(7.1) | 206.2(2.4) |
| d | | 271.2(1.5) | 124.9(1.5) | 49.2(3.6) | | |
| 689.3[c] | $5s^2\ ^1S_o - 5s5p\ ^3P_1$ | 351.2(1.4) | 164.0(0.8) | 62.5(1.0) | | |
| e | | 351.2(1.8) | 163.7(1.0) | 62.3(1.4) | | |
| 293.2[f] | $5s^2\ ^1S_o - 5s6p\ ^1P_1$ | 474.06(5) | 224.73(5) | 93.62(6) | 25.8(5) | 79.7(3) |
| b | | 475.4(7) | 226.3(7) | 95.2(1.0) | | |
| 295.2[b] | $5s^2\ ^1S_o - 5s6p\ ^3P_1$ | 423.8(3.2) | 199.6(4) | 80.7(6) | | |
| 242.8[g] | $5s^2\ ^1S_o\ 5p4d\ ^1P_1$ | 600.1(9) | 285.0(8) | 123.7(8) | | |
| 730.9[h] | $5s4d\ ^1D_2 - 5p4d\ ^1D_2$ | 289(7) | 130.0(1.2) | 49.0(1.5) | | |
| 716.7[h] | $5s4d\ ^1D_2 - 5s6p\ ^1P_1$ | -463.2(1.0) | -220.6(1.0) | -99.5(1.0) | | |

a. Borghs et.al. /Bor.83/
b. Eliel et.al. /Eli.83/
c. Buchinger et.al. /Buc.85/
d. Martin et.al. /Mar.86/
e. Bender et.al. /Ben.84/
f. This experiment
g. Foot et.al. /Foo.84/
h. Grundevik et.al. /Gru.83/

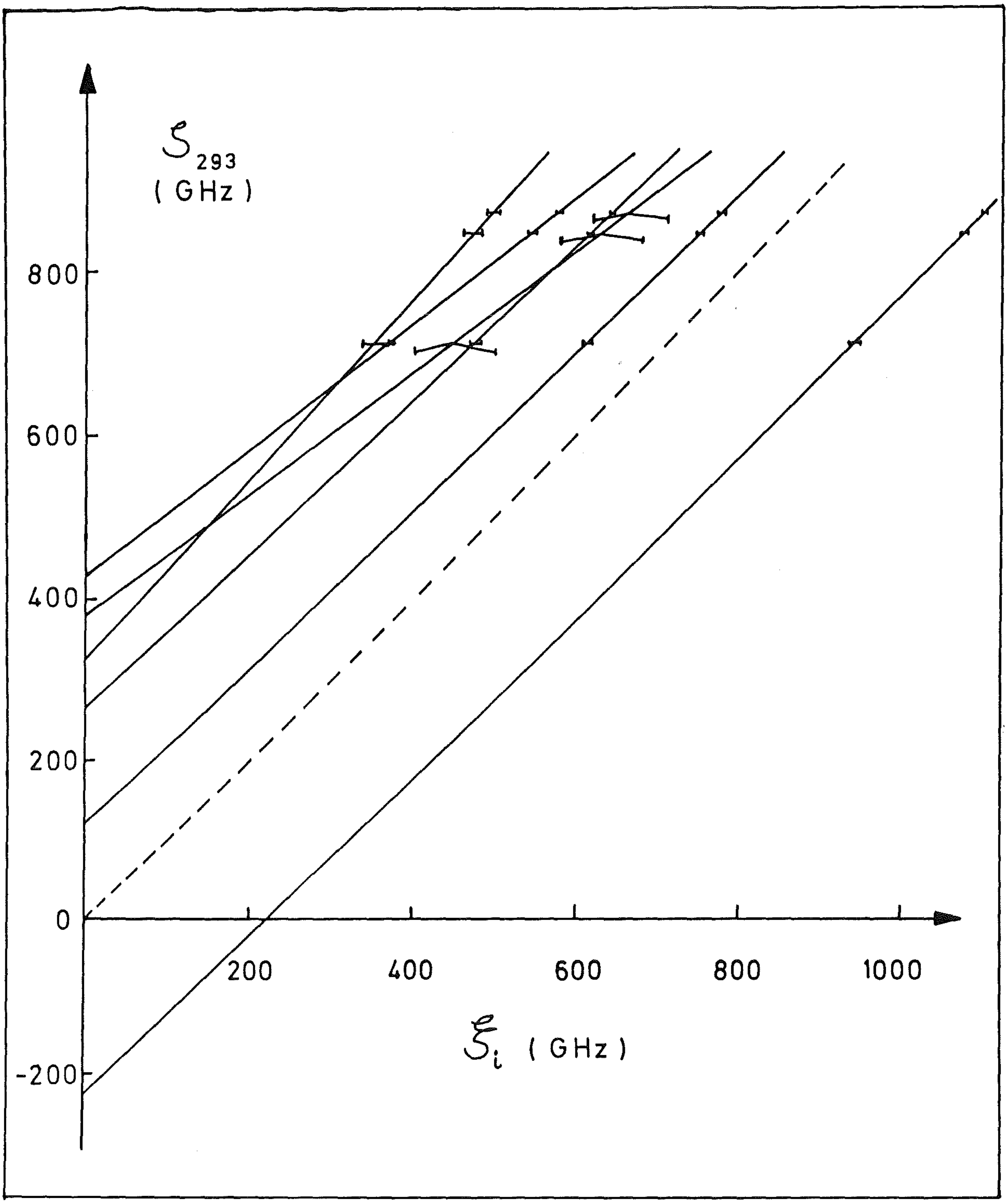

**Fig. 5.3** The King plot of the measured isotope shifts versus the shifts in line 293.2 nm. The dot line is plotted to guide the eyes for the unity slope.

Table **5.2** The evaluated electronic factor ratios (slopes) and the intercepts from the King plot procedure

| Line (nm) | Reference | Slope $F_{293}/F_i$ | Intercept $M_{293}-M_iF_{293}/F_i$ |
|---|---|---|---|
| 421.6 | /Bor.83/ | 0.74(20) | 381(81) |
| 460.7 | /Eli.83/ | 1.10(15) | 326(16) |
| 689.3 | /Buc.85/ | 0.94(12) | 269(3) |
| 295.2 | /Eli.83/ | 0.97(10) | 120(5) |
| 242.8 | /Foo.84/ | 0.99(7) | -224(29) |
| 730.9 | /Gru.83/ | 1.03(15) | 432(53) |
| 716.7 | /Gru.83/ | -1.73(18) | -604(95) |

**The results of the isotope shift of 293.2 nm transition are compared with the other transitions in Fig.5.3. The dashed line is plotted to guide the eyes for the unity slope. The graphs show that the isotope shifts are consistent and yield the results of electronic factors as presented in Table 5.2. It can be seen that all slopes are approximately parallel to the unity slope (dashed line), which means that the electronic factors ($F_i$ values) are quite similar. But the slope of the ionic state SrII (421.6 nm) shows the electronic factor is 1.35 times larger than for 293.2 nm line. Not shown, but given in Table 5.2 is the unusual slope of the 716.7 nm line. Its negative slope is results from the negative shifts of the isotopes, whereas the lighter isotopes shift to the higher frequencies. The electronic factor ($F_i$ value) of this line is so small about 0.58 times to the 293.2 nm line, which means the electric field gradiens are different and the field shifts should be expected very different. This low value shows that either the SrII or SrI (293.2 nm), if not both, is not such a simple spectrum as might be expected.**

### 5.1.4. Electronic Factor Calibration

The electronic factors F and M were derived from $\delta\langle r^2\rangle$ values of stable strontium isotopes, resulting from an analysis of muonic X-ray studies. There are two different sets of such data available. The first set:

$$\langle r^2\rangle^{86} - \langle r^2\rangle^{88} = +0.047(6)\ \mathrm{fm}^2,$$

$$\langle r^2\rangle^{86} - \langle r^2\rangle^{87} = +0.040(4)\ \mathrm{fm}^2,$$

$$\langle r^2\rangle^{84} - \langle r^2\rangle^{86} = +0.063(7)\ \mathrm{fm}^2$$

adopts the results of Bender et. al./Ben.84/. The three values were treated as independent data. This set leads to $F = -1.08(40)\ \mathrm{GHz/fm}^2$ and $M = +660(80)$ GHz.

The second set was derived from preliminary values of Barret equivalent radii $R_{k\alpha}$ determined by recent muonic X-ray experiments from /Fri.86/: $R^{86}_{k\alpha} - R^{88}_{k\alpha} = +0.0088(10)$ fm and $R^{84}_{k\alpha} - R^{86}_{k\alpha} = +0.0130(10)$ fm. The value of parameter k was 2.167, and $\alpha$ has the value 0.0943 $\mathrm{fm}^{-1}$ .

With these input data and an $R^{88}_{k\alpha}$ of 5.0483 fm, the $\delta\langle r^2\rangle$ were computed using standard formulas /Eng.74/ and assuming a two-parameter Fermi charge density with a skin thickness paramater t fixed to 2.20 fm. The radius parameter c was adjusted in a way that the Barret moment differences for the Fermi distribution reproduced the muonic Barret moment differences; these in turn were recalculated from the given $\delta R_{k\alpha}$ as the Barret moment differences of homogeneously charged spheres with radii differing by $\delta R_{k\alpha}$. The resulting set 2 is:

$$\langle r^2\rangle^{86} - \langle r^2\rangle 88 = +0.058(7)\ \mathrm{fm}^2,$$

$$\langle r^2\rangle^{84} - \langle r^2\rangle 86 = +0.085(7)\ \mathrm{fm}^2,.$$

The uncertainties quoted are those arising from the $\delta R_{k\alpha}$ errors only. The electronic factors F and M then become: $F = -0.58(24)\ \mathrm{GHz/fm}^2$, $M = +725(65)$ GHz.

Using either $\delta\langle r^2\rangle$ set, two different evaluations were performed to deter-

**mine $\delta<r^2>$ for all isotopes. Instead of using F and M values given above, it is advantageous to go back to the calibrating $\delta<r^2>$ data. They define a King line /Kin.84/, and the $\delta<r^2>$ are found in a least square procedure that ensures that the resulting uncertainties are minimised. The results of the optical isotope shifts from this measurement and the mean square charge radius differences $<r^2>^A - <r^2>^{88}$ are given in Table 5.3. The evaluation was done with two different sets of calibration data from set 1 /Ben.84/ and set 2 /Fri.86/ and the results are displayed in Fig.5.4a and in Fig.5.4b. In view of the calibration problem it is not surprising that these results differ somewhat from others as e.g. /Buc.85/ , /Mar.86/ and /Eas.87/. King plot method.**

Table 5.3 Optical isotope shifts and mean square charge radius changes for strontium nuclei.

| Mass Number A | Isotope shift (MHz) | $\langle r^2\rangle^A - \langle r^2\rangle^{88}$ ($fm^2$) | |
|---|---|---|---|
| | | Set 1 | Set 2 |
| 80 | -992(5) | +0.227(20) | +0.294(21) |
| 81 | -881(4) | +0.217(14) | +0.294(13) |
| 82 | -728.4(5) | +0.169(13) | +0.220(15) |
| 83 | -610.9(2) | +0.149(10) | +0.200(15) |
| 84 | -474.06(5) | +0.110(9) | +0.143(10) |
| 85 | -314.8(2) | +0.047(14) | +0.042(28) |
| 85m | -338.8(1.4) | +0.070(9) | +0.084(12) |
| 86 | -224.73(5) | +0.047(5) | +0.058(7) |
| 87 | -93.62(6) | +0.007(7) | +0.002(15) |
| 87m | -85(8) | -0.001(10) | -0.02(2) |
| 88 | 0 | 0 | 0 |
| 89 | -25.8(5) | +0.10(4) | +0.21(10) |
| 90 | -79.7(3) | +0.23(9) | +0.46(22) |

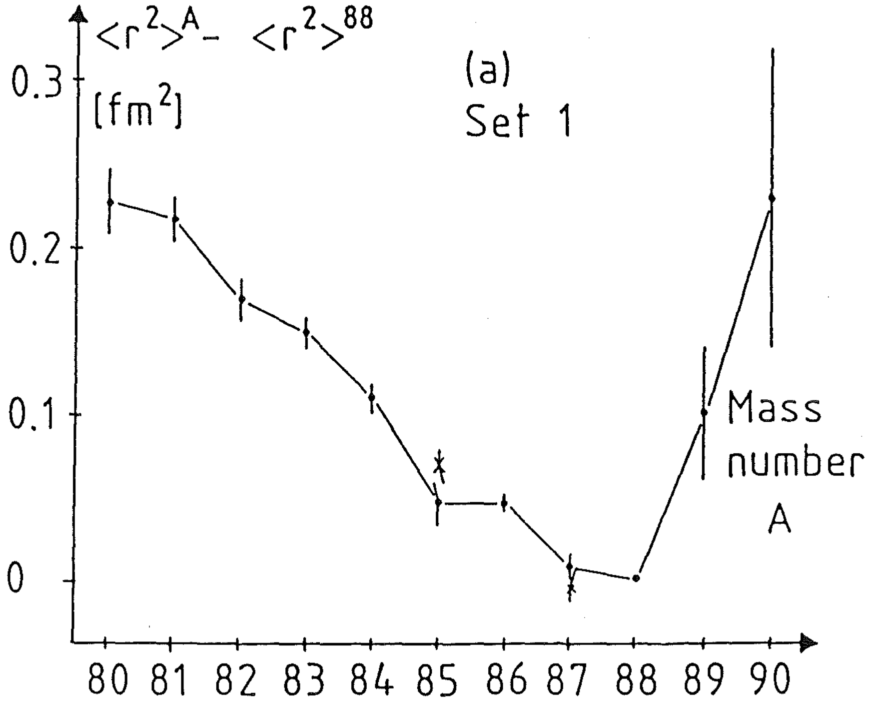

**Fig. 5.4a** The evaluated ms nuclear charge radius difference from $<r^2>^{88}_{N=50}$ with /Ben.84/ as reference

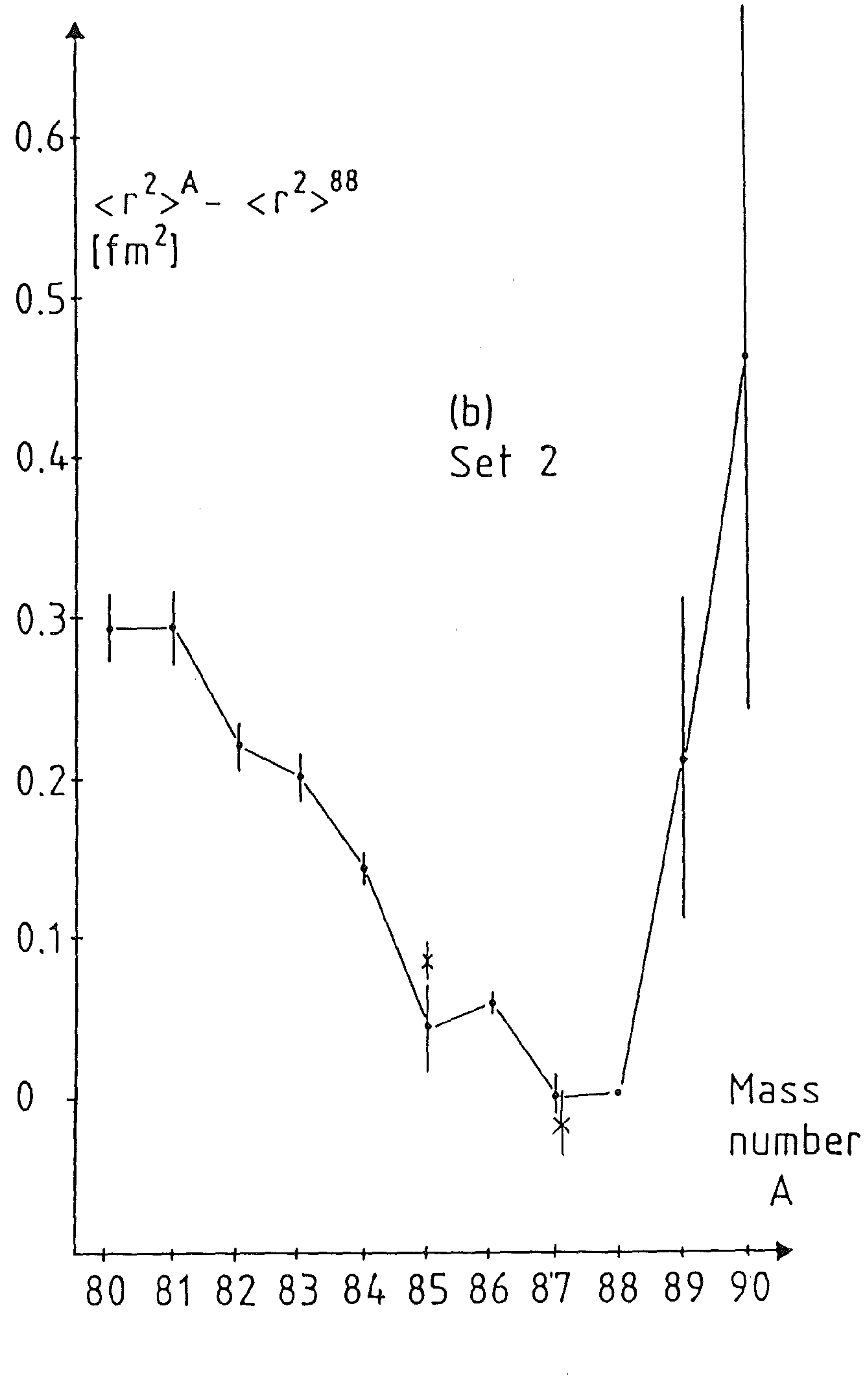

**Fig. 5.4b** The evaluated ms nuclear charge radius difference from $<r^2>^{88}_{N=50}$ with /Fri.86/ as reference

## 5.2. Hyperfine Structures and Nuclear Moments

### 5.2.1. Hyperfine Structure

The hyperfine structure effects are responsible for the splittings of the atomic energy levels. These effects result from the fact that a nucleus posesses electromagnetic multipole moments of higher order than the electric monopole and interacts with the electromacnetic field produced at the nucleus by the electrons. By using general symmetry arguments of parity and time reversal invariance, it is shown that the number of possible multipole ($2^k$ poles) moments is restricted /Sob.72/. These are the magnetic moments for odd k and the electric moments for even k, i.e. the magnetic dipole $\mu$ (k=1), electric quadrupole Q (k=2), magnetic octupole $\Omega$ (k=3), electric hexadecapole (k=4), and so on. The most important of these moments are the magnetic dipole moment, which associated with the nuclear spin and the electric quadrupole moment, which caused by the departure from a spherical charge distribution in nucleus. Interaction of the higher order multipole moments ($k>2$) with the electron is interesting but often negligibly small.

For the nuclei with nonzero moments $\mu_I$ and Q, an additional interaction with the electron shell take place and produces a splitting in the energy of the fine structure levels. The energy of these hf multiplets is given by the traditional Casimir formula:

$$W_F = W_J + W_\mu + W_Q \tag{5.14}$$

$$= W_J + \frac{AC}{2} + B \cdot \frac{3C(C+1) - 4I(I+1)J(J+1)}{8I(2I-1)J(2J-1)} \tag{5.15}$$

where $W_J$ is the fine structure energy, $W_\mu$ and $W_Q$ are, respectively, the magnetic dipole and the electric quadrupole interaction energy. A is the interval constant or the magnetic dipole constant and B is the electric quadrupole constant. $C = F(F+1)-J(J+1)-I(I+1)$, where I is the nuclear spin, j is the total angular momentum of the shell electrons and F is the total angular momentum for the different hfs states.

### 5.2.2. Nuclear Moments

The magnetic dipole interaction constant A and the electric quadrupole interaction constant B of the 5s6p $^1p_1$ state of strontium have been derived from the observed hyperfine structure of the odd A isotopes by means of the Casimir formula (5.15). The values of the hyperfine interaction constants A and B are listed in Table 5.5, comparing to the previous measurements of $^{87}$Sr by Eliel et.al. /Eli.83/ and Grundevik et.al./Gru.83/, they are in good agreement with our values. The errors quoted are those arising from the uncertainties in the experimental data and the overall errors concerning statistics.

The characteristics of nuclides i.e. nuclear magnetic dipole moment $\mu_I$ and electric quadrupole moment $Q_s$ could be straightforward calculated from A and B, respectively. Therefore the calculation of the magnetic dipole moments is available, using the ratio of A factors, the known nuclear spins and then scaling to the known value of magnetic dipole moment of one isotope, $\mu_x = \mu.I.A_x/A.I_x$. It is assumed that the dominant contribution to the magnetic dipole moments from the $\pi 1p_{3/2}$ proton in the range of isotopes A = 80–90 is rather similar nuclear structure and thus a small hyperfine anomaly.

The known value of $\mu_I$ can be obtained from the Table of Isotopes /Led.78/ and from the compilation of G.H. Fuller and V.W. Cohen /Ful.69/. A.G. Kucheriav et.al. /Kuc.58, Kuc.59/ had applied the molecular beam magnetic resonance (MBMR) method and had obtained $^{87}\mu = -1.0924(9)$ nm. The method of nuclear resonance (NMR) was applied by Bank and Schwenk /Ban.73/ and was refined again by Sahm and Schwenk /Sah.74/ with the result of −1.089274(7) nm. This result is quoted in /Led.78/ as −1.093602(1) nm due to the correction of a new value of the proton moment. We used the value $^{87}\mu = -1.0924(7)$ nm with diamagnetic correction from L. Olschewski /Ols.72/ as the reference. This value was obtained from the rf transitions between the Zeeman levels of the ground state $^1S_0$ by using the optical pumping method. Because the beam consisted of strontium atoms, intramolecular interactions and the chemical shift effects as in NMR method could be disgarded and the diamagnetic correction could be evaluated accurately.

The spectroscopic electric quadrupolemoments $Q_s$ can be deduced from the ratios of the measured quadrupole interaction canstants B by using the relation: $Q_x = Q_A.B_x/B_A$, where $Q_A$ is the known quadrupole moment value of isotope A with respect to the hf interaction constant $B_A$. G. zu Putlitz /zuP.63/ had investigated the hfs of the 5s5p $^3P_1$ state of the SrI spectra by the optical double resonance method and obtained the electric quadrupole moment of $Q_{87}$ = +0.36(3) barn. This value was applied to calculate the quadrupole moments for the measured hfs of the $^3P_2$ state of $^{87}$Sr, using the atomic beam magnetic resonance (ABMR) technique by S.M. Heider and G.O. Brink /Hei.77/. The average value from the electronic states was obtained $Q_{87}$ = +.335(20) b. This value was been corrected for the antishielding effects due to polarization of the core electrons by Sternheimer. The deduced values of the magnetic dipole moment and the electric quadrupole moment are shown in Table 5.4.

The theoretical ab initio method was applied to evaluate the nuclear electric quadrupole moments for $^{87}$Sr by Grundevik et.al./Gru.83/ The effective radial quadrupole parameters $<r^{-3}>$ have been calculated by using the Hartree Fock (HF) and the relativistic Hartree Fock (RHF) methods. This yielded the quadrupole moments of the two states: Q(5s6p $^1P_1$) = 0.63 b and Q(5s4d $^1D_2$) = 0.70 b. These values are not reliable and should be deduced with more detailed calculations as the states involed are very strongly perturbed.

Table **5.4.** Hyperfine splitting constants A and B as calculated from the component positions for odd Sr isotopes and isomers. The nuclear magnetic dipole moments $\mu_I$ and the electric quadrupole moments Q were derived from A and B factors.

| Mass Number A | Nucl. Spin I | A Factor (MHz) | B Factor (MHz) | $\mu_I$ ($\mu_N$) | Q (b) |
|---|---|---|---|---|---|
| 81 | 1/2 | -681(6) | - | +0.540(5) | - |
| 83 | 7/2 | +149.02(6) | +31.6(5) | -0.8289(7) | +0.823(50) |
| 85 | 9/2 | +139.75(4) | +12.4(3) | -0.9994(7) | +0.323(20) |
| 85m | 1/2 | -753.3(2.2) | - | +0.599(2) | - |
| 87 | 9/2 | +152.750(15) | +12.87(15) | -1.0924(7) | +0.335(20) |
| 87m | 1/2 | -990(12) | -12.1(5) | +0.787(9) | - |
| 89 | 5/2 | +288.65(20) | | -1.147(2) | -0.314(23) |

## 6. DISCUSSION

### 6.1. Nuclear Models

Theoretical aspects for the calculation of nuclear size can be started from the usual liquid drop model (LDM) /Wei.35/. Analogous to the drops of liquid, nuclei are incompressible homogeneously charged spheres with radii expressed as $R = r_o A^{1/3}$ , where $r_o$ is radius constant of about 1.2 fm. For practical reasons, it is often presented in terms of the second radial moments, the mean square (ms) radius

$$< r^2 >= 3/5 r_o^2(A) A^{2/3} \tag{6.1}$$

The $r_o(A)$ varies slowly with A,e.g. /Col.67/,

$$r_o = 1.15 + 1.80A^{-2/3} - 1.20A^{-4/3} \tag{6.2}$$

Due to the simplicity, this model can serve as useful standard for comparison with experimental data.

Myers et.al./Mye.77, Mye.80, Mye.83/ had developed the liquid drop model by considering terms of nuclear density distribution including neutron skin thickness, nuclear deformations and bulk redistributions of nucleon. With this droplet model (DM) the ms radius can be calculated from the expression

$$< r^2 >=< r^2 >_u + < r^2 >_r + < r^2 >_d \tag{6.3}$$

where the three terms are the contributions from the size of the uniform distribution, the redistribution with its shape dependence and the last term, the nucleon diffuseness, respectively. This model prediction with deformation corrections included, shows in general good agreement with the measured values. Poor agreement is obtained when applied to rubidium isotopes (Z=37), especially for the neutron deficient side ( N<50 ). The discrepancy can be accounted for by the larger values of zero-point quadrupole deformation other than the static deformation expected as suggested by Campi and Epherre /Cam.80/.

A density dependent Hartree-Fock (DDHF)-BCS method /Eph.81/ was applied to calculate neutron separation energies and ms charge radii of $^{74-104}$Kr and $^{76-106}$Sr. They are in excellent agreement with experimental values for N>50. On the contrary, for the neutron deficient isotopes N<50, the discrepancy can be accounted for by the large zero-point quadrupole vibration effect.

One of the sensibly interesting theoretical models, the two parameter Fermi distribution is proposed recently by Wesołowski /Wes.85/. A spherically symmetric distribution of charge in deformed and diffused surface nucleus under rotation is assumed. Many factors are taken into account, the proton and neutron odd-even effect, the neutron shell effect, the deformation effect and the effect of N–Z assymmetry of nuclei. Attempts have been made to empirically a global behavior of the parameters of the charge distributions which is seen much more clearly than the Hartree-Fock and droplet model calculations. The comparision of the model prediction values with the experimental ones shows a very good agreement, especially the negative shift in the case of neutron deficient strontium isotopes. The ms charge radii can be reproduced fairly well as shown in Fig.6.1.

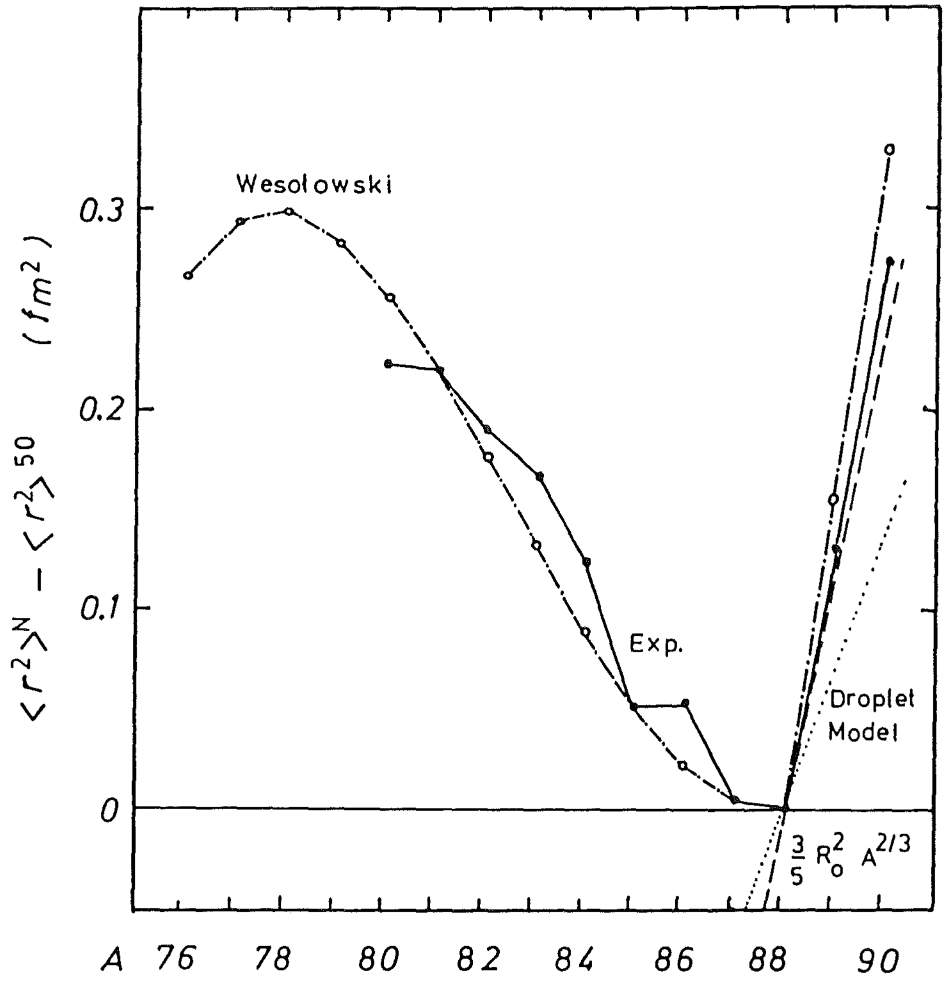

Fig. 6.1 The evaluated ms nuclear charge radius variation compared with the theoretical values from Wesołowski /Wes.85/

## 6.2. Nuclear Deformations

The experimental result of ms charge radii of the strontium isotopic sequence shows a distinct nuclear shrinking before neutron shell closure N=50. The dot line in Fig.6.1 gives the calculated values of $\delta<r^2>$ using the spherical droplet model /Mye.77/. The departure of the experimental curve from the calculated one can be expressed in terms of nuclear deformation. In this attempt, the experimental values of $\delta<r^2>$ are reproduced as a function of deformation parameter ($\beta$) by the empirical droplet model as describes:

The simple incompressible fluid model of the nucleus is generally used to correlate the variation of $<r^2>$ with two effects when neutrons are added, i.e. i) an increasing in the volume of the charge distribution and ii) changing of the nuclear charge at the constant volume and density. The ms nuclear charge radius is then expressed as:

$$< r^2 >=< r^2 >_{sph} (1 + \frac{5}{4\pi} < \beta^2 >) \qquad (6.4)$$

where $<\beta^2>$ is the ms deformation of nucleus in the ground state /Hei.74/.

The total change in $<r^2>$ between two neighboring A and A′ can be expressed by:

$$\delta < r^2 >^{AA'}= \delta_{sph} < r^2 >^{AA'} + \frac{5}{4\pi}\delta[< r^2 >_{sph}< \beta^2 >]^{AA'} \qquad (6.5)$$

since $<\beta^2>$ is usually small compared to unity, the approximate result is then:

$$\delta < r^2 >^{AA'}= \delta_{sph} < r^2 >^{AA'} + \frac{5}{4\pi} < r^2 >_{sph} \delta < \beta^2 > \qquad (6.6)$$

Insofar as the field shift is proportional to $\delta<r^2>$ it can be expressed as the sum of two terms, one depending on changes in nuclear volume (volume shift) and the other depending on the nuclear shape (shape shift) or deformation.

In order to extract $\delta<\beta^2>$ from the observed $\delta<r^2>$, one has to evaluate the $\delta_{sph}<r^2>^{AA'}$ from the spherical droplet model data as compiled by Myers /Mye.81/.

The nuclear deformation behaviors on both sides of beta stability region can be studied by gamma ray spectroscopic methods. The energy and half-life systematics of the nuclear lying states suggest a shape and size of nuclear deformation and have been interpreted as arising from collective quadrupole motion of nucleus. A collective model proposed by Bohr and Mottelsson /Boh.75/ has been extremely successful in describing many aspects of nuclear shapes. In Fig.6.2 the systematics of the first excited $2^+$ state energies of even-even strontium nuclei are plotted /Led.78/. The shell closure at the magic number N=50 is clearly observed in the highest lying $2^+$ state for $^{88}$Sr isotope. It reveals a marked drop in the energy levels as one moves away from N=50 and strongly supports a new region of large deformation centred around N = Z = 38. This region is very interesting since the highest value of quadrupole deformation $\beta = 0.4$ has been found experimentally /Nol.74, Ham.81/. For theoretical grounds, N=Z=38 exhibits the shell gaps effect of both neutrons and protons which would reinforce each other and drive a nucleus towards large deformed shape.

A phenomenological description of the nuclear collective model is the differentiation of the permanent (static) deformation and the dynamic (vibrational) deformation. The current studies of the Coulomb excitations or the inelastic electron scattering experiments yield the gamma ray spectroscopic results, in which the quantitative information on deformation parameter can be obtained from the measured reduced E2 transition probability from the relation; /Ste.65/,

$$< \beta^2 >= \frac{B(E2, 0^+ \rightarrow 2^+)}{(3ZR^2/4\pi)^2} \tag{6.7}$$

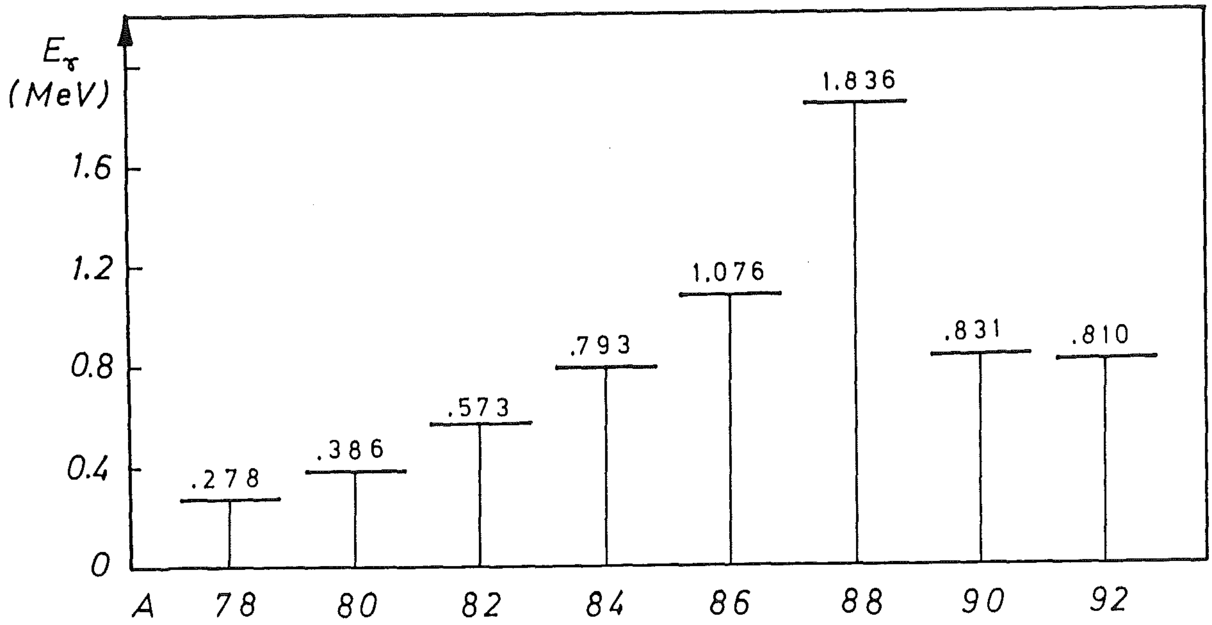

**Fig. 6.2** The excitation energies of the first $2^+$ levels of even strontium nuclei from A = 78 to 92

where $R = 1.2A^{1/3}$ fm. The B(E2) value between the $0^+$ ground state and the first $2^+$ state in even-even nuclei represents the occurrence of the quadrupole distortions in nuclei /Chr.72/ and relates to the intrinsic quadrupole moment $Q_o$ by:

$$B(E2, 0^+ \rightarrow 2^+) = \frac{5}{16\pi} Q_o^2 \tag{6.8}$$

The reduced transition probability can be roughly estimated from the energy of the first $2^+$ level by using the general empirical rule /Gro.62/,

$$B(E2, 0^+ \rightarrow 2^+) = \frac{(12 \pm 4)10^{-3} Z^2}{A E_{2^+}} \tag{6.9}$$

The experimentally measured reduced E2 transition probability $B(E2, 0^+ - 2^+)$ values and the deduced deformation parameter $\delta\langle\beta\rangle^{88,A}$ are given in Table 6.1. The B(E2) values are taken from the compilation in Nuclear Data Sheets /Bun.76, Tep.78, Mül.79/ and for $^{78,80}$Sr were calculated from the data of the intrinsic quadrupole moments /Lis.82/. In general, the results of the various investigations are in satisfactory agreement. As is apparent from Fig.6.3, the nuclear deformation decreases with increasing neutron number, being smallest for $^{88}$Sr with a closed neutron shell.

Table 6.1 The transition probability values, $B(E2, 0^+ - 2^+)$ and the extracted ms deformation parameters from the collective model and from the semi-empirical droplet model

| A | $B(E2, 0^+ - 2^+)$ | $\beta$ | $\delta\langle\beta^2\rangle^{A-88}_{CM}$ | $\delta\langle r^2\rangle^{A-88}_{exp}$ | $\delta\langle\beta^2\rangle^{A-88}_{DM}$ |
|---|---|---|---|---|---|
| 78 | 1.08(13) | 0.436 | 0.178(23) | - | - |
| 80 | 0.88(9) | 0.387 | 0.138(15) | 0.227(20) | 0.117(8) |
| 82 | 0.500(25) | 0.286 | 0.070(4) | 0.169(13) | 0.081(6) |
| 84 | 0.285(30) | 0.213 | 0.033(5) | 0.110(9) | 0.052(4) |
| 86 | 0.118(16) | 0.134 | 0.006(3) | 0.047(5) | 0.025(3) |
| 88 | 0.082(2) | 0.110 | 0 | 0 | 0 |
| 90 | 0.232(70) | 0.184 | 0.020(10) | 0.23(9) | 0.016(6) |

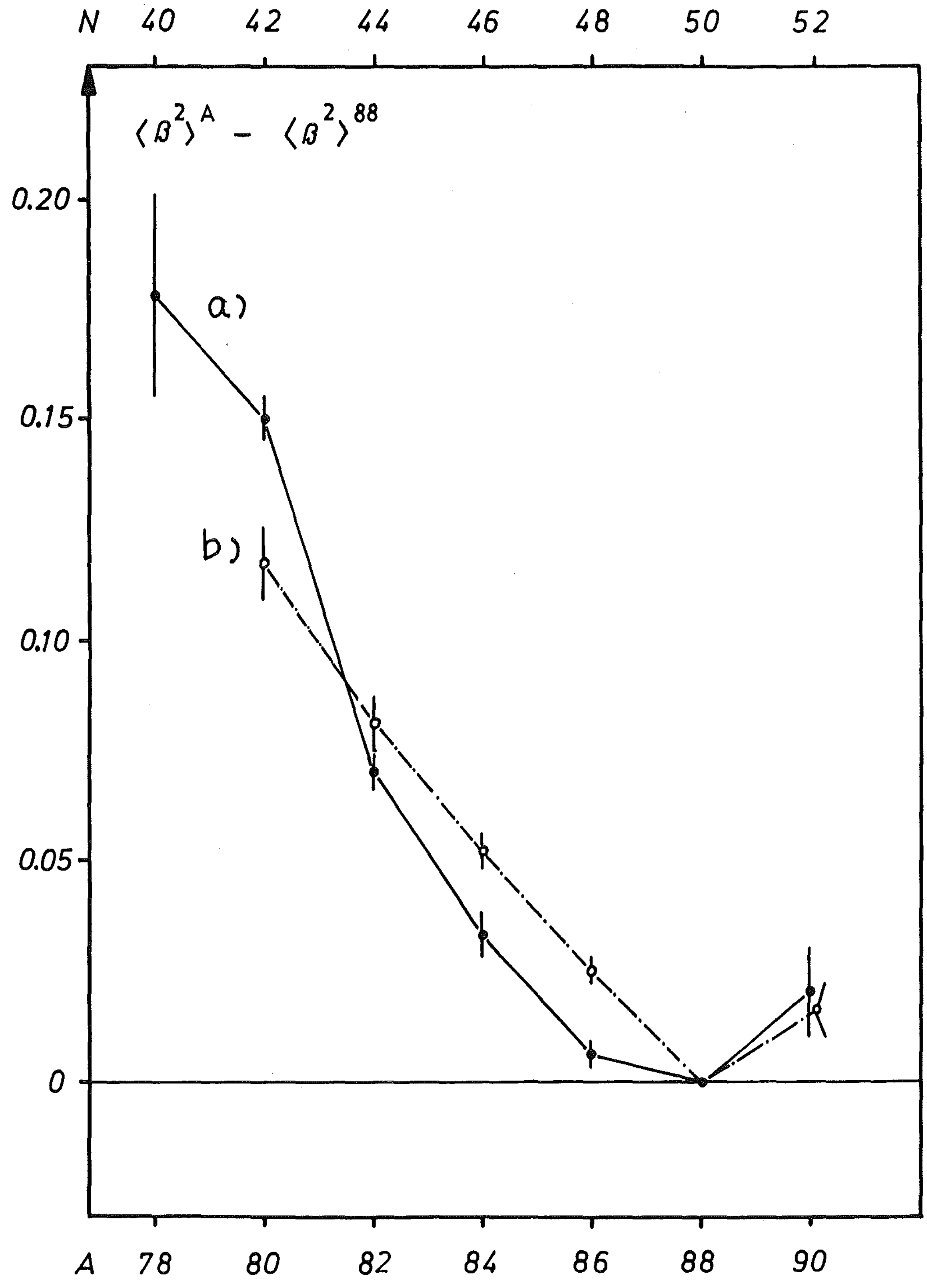

**Fig. 6.3** The variations of ms deformation from $^{88}$Sr nucleus which were deduced from a) B(E2,0$^+$ –2$^+$) values and b) semiempirical droplet model

## 6.3. Comparison of MS Charge Radii with Neighboring Elements

Fig.6.4. compares the trend of $\delta<r^2>$ for strontium isotopes observed from the present work is comparable to those for krypton (Z=36) /Ger.79a/, rubidium (Z=37) /Thi.81/, zirconium (Z=40) /Hei.63/ and molybdenum (Z=42) /Auf.78/. The subsequent addition of neutrons to fill the ($1g_{9/2}$) neutron shell results in regular decrease of the ms charge radius in the successive isotope shifts. An obvious shell crossing effect is apparent, as shown by the abrupt increase in $<r^2>$. This is due to the proton core polarization by adding neutrons, indicating a strong systematic shell effect. By comparison $\delta<r^2>$ values between these isotopes, all values depend on neutron numbers, but the variation is not monotonic, as shown by the staggerred lines.

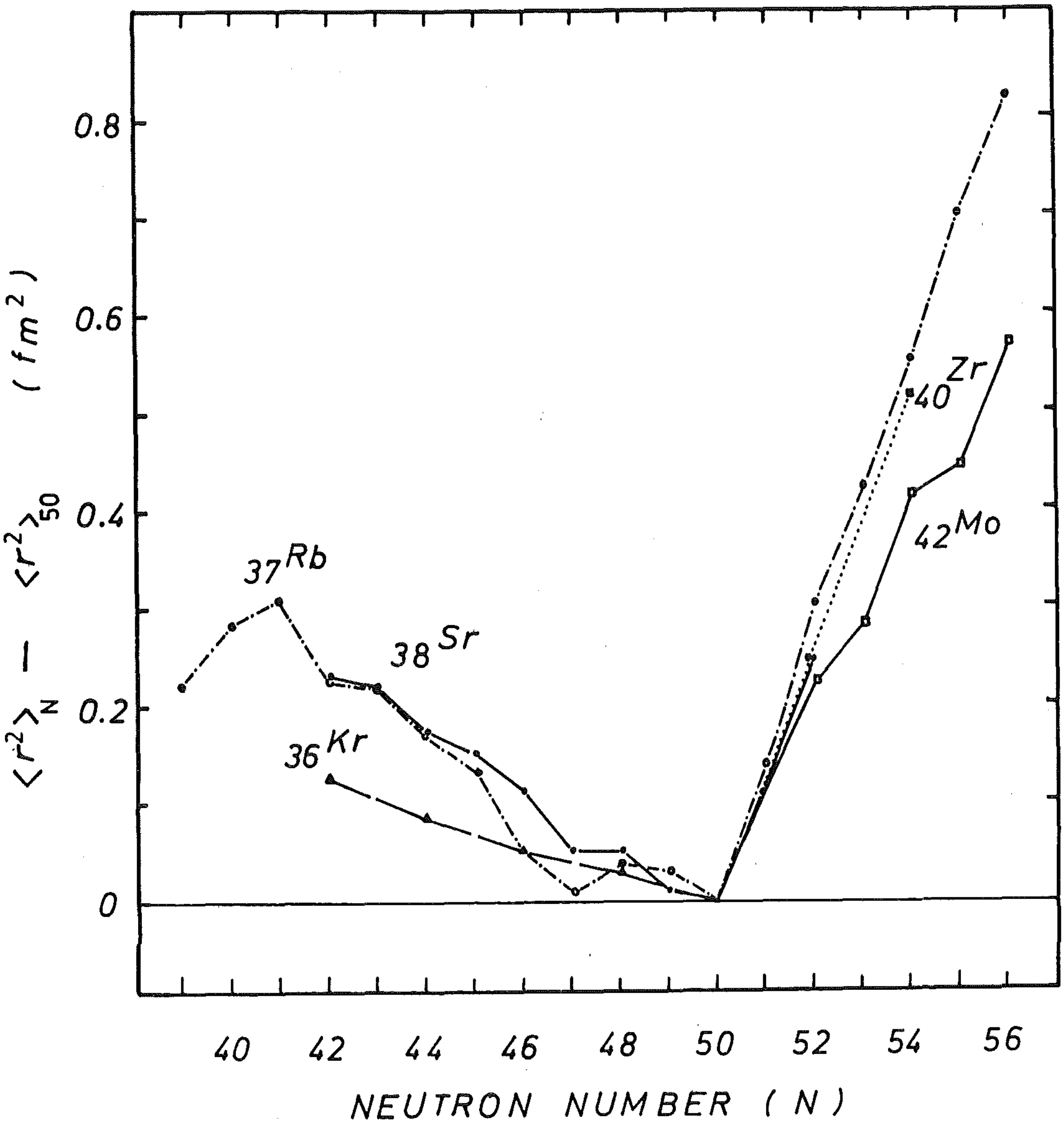

Fig. 6.4 The ms nuclear charge radius variation as different from $<r^2>_{N=50}$ for Krypton, Rubidium, Strontium, Zirconium and Molybdenum

### 6.4. Odd Even Staggering

It is found from the isotope shift measurements that the center of gravity of the hfs energy levels for odd A nucleus does not lie half-way between the corresponding energy levels of the neighbouring even isotopes /Kuh.69/. The extracted ms charge radii of odd A nuclei often appear to be smaller than the mean size of the neighbouring even A nuclei. It is traditional to express the degree of the odd even staggering (OES) through:

$$\gamma = \frac{2 \cdot [< r^2 >^A - < r^2 >^{A-1}]}{< r^2 >^{A+1} - < r^2 >^{A-1}} \tag{6.10}$$

where A is an odd mass number corresponding to the ms nuclear charge radius. The odd even staggering parameter ($\gamma$) can also be expressed more directly by the more accurate isotope shift data /Ans.86a/ as:

$$\gamma = \frac{2 \cdot [\delta\nu^{A-1,A} - M/A(A-1)]}{\delta\nu^{A-1,A+1} - 2M/[(A-1)(A+1)]} \tag{6.11}$$

which differs from the last equation in that the electronic parameter $F_i$ and its uncertainty are eliminated.

The theoretical explanations of these staggering effect as a nuclear deformation phenomenon were given by Wilets et. al. /Wil.53/ , Bodmer /Bod.54/ and Tomlinson and Stroke /Tom.68/. They expected that the even-even nuclei were somewhat more deformed than the odd-even nuclei. Sorensen et. al. /Sor.66/ suggested that the OES was due to a blocking of ground state quadrupole vibrations of the nucleus by the odd neutron. Reehal and Sorensen /Ree.71/ used the pairing plus quadrupole model to explain the blocking effect of the odd particle for the different behavior of the OES. Zawischa /Zaw.80/ has extended this idea by taking into account the short range attraction between neutrons and protons to explain the OES of the rare earth nuclei. Talmi /Tal.84/ had studied the polarization of the proton core by valence neutrons as a possible mechanism for producing the odd-even variation in the charge radii of isotopes.

In Fig.6.5. values of the staggering parameter of the Sr nuclei are plotted against the neutron number. An inversion of the staggering occurs for A=85 and 87, whose ms radii are also less than half of the corresponding neighboring even isotopes. For A=81 and A=83 the inversion can be interpreted as a nuclear deformation staggering, with the transition from a slightly deformed to a strongly deformed oblate shape. Gamma spectroscopy of the neutron deficient $^{78,79,80}$Sr has yielded evidence for a coexistence and crossing of the bands in these nuclei /Lis.78/.

The behavior of the OES effect after closed neutron shell is of interest, especially for the isotopes with magic-plus-one neutron number. It is established that the OES effect disappears after N = 28, 50,82 and 126 as has been plotted together in Fig.6.4 /Auf.83/. It is known that such nuclei represent isotopes with special stability. A reasonable explanation for this is given by the theory of Zawischa /Zaw.80/, in which a blocking of pairing correlations reduces the ms neutron radius by reducing the diffuseness of the Fermi edge for neutrons. Proton-neutron interaction makes the proton distribution follow the neutron density. Therefore, after magic shells, only a small OES is to be expected.

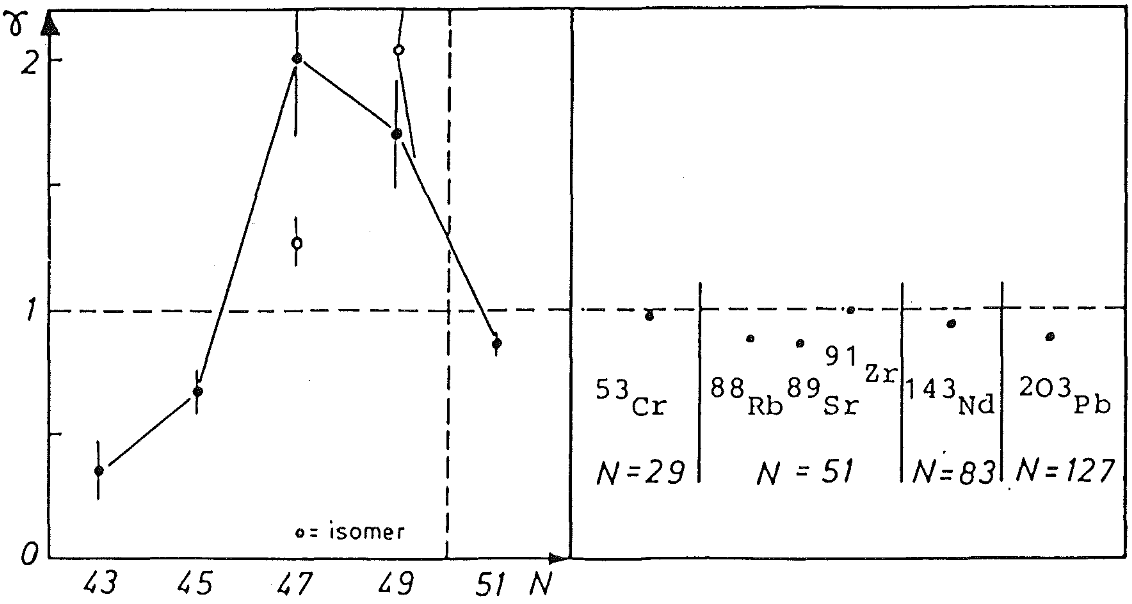

**Fig. 6.5** The extracted odd even staggering parameter of the strontium nuclei and of the magic plus one nuclei

**An alternative representation of the odd even staggering effect can be given by the expression /Ans.86/:**

$$\Delta = \delta < r^2 >_{A,88} - \frac{1}{2} \cdot [\delta < r^2 >_{A-1,88} + \delta < r^2 >_{A+1,88}] \qquad (6.12)$$

$$= \delta < r^2 >_{A,A+1} + \delta < r^2 >_{A,A-1} \qquad (6.13)$$

**As plotted in Fig.6.6. The strontium data are taken from set 1 of this experiment and extend further to the lower mass number at A = 79 and 80 from the recent data of /Eas.87/. The error limits are determined from the total errors of $\delta$<r$^2$> in which the dominant systematic errors are included. The large error at the point A = 88 is due to the large total errors of the both neighbouring isotopes A = 87 and 89. The small errors at A = 80, 82 and 83 are due to the similarity of error limits for all the three isotopes A, A–1 and A+1 as shown in equations (6.12) and (6.13) which hence reduces systematically the error limits of $\Delta$. The other graphs show the deduced values of $\Delta$ for tin (Sn), which are taken from the data /Ans.86b, Loc.87/ and also for lead (Pb) data /Ans.86/.**

**The graph exhibits the differences of Sr from the normal odd even staggering as in the case of tin and lead. The anomalous odd even staggering occurs at the region A < 83 through the lower mass number to A = 79, i.e. the $\Delta$ values are positive for odd A and negative for even A. This inverse odd even staggering might be somewhat correlated to the strongly deformed shape of nuclei in this region. When considering the total trend of $\Delta$ , at the negative part, it seems to be highest at A = 88 and gradually increases along the lower mass numbers and reaches zero at A = 80. The upper part, the positive values are quite constant in the range between +0.01 to +0.02 in the same manner as for the tin isotopes. The range of $\Delta$ for the lead isotopes are enlarged betseen 0.01 to 0.04 for both the positive and negative parts.**

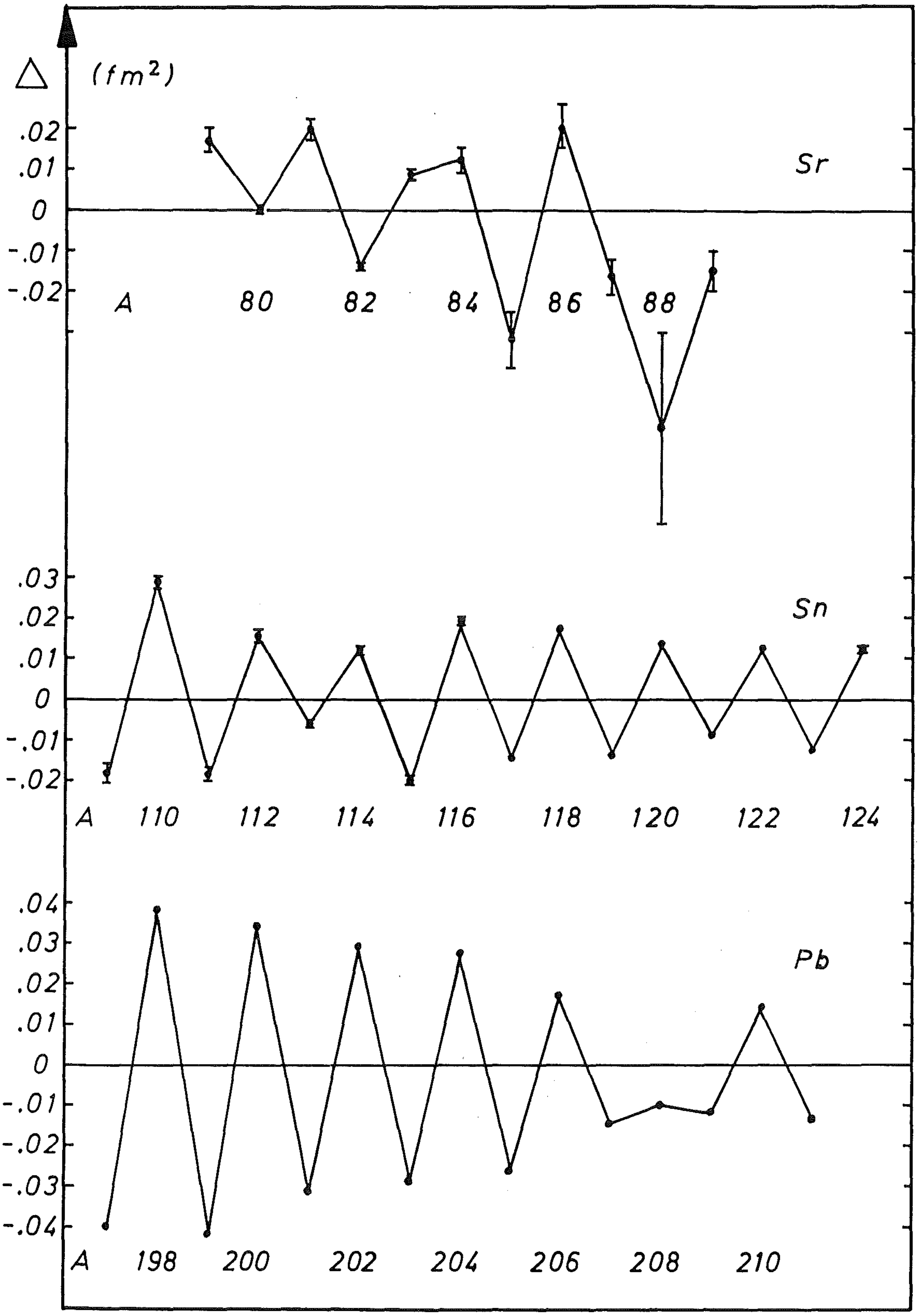

Fig. 6.6 **Odd even staggering parameter (Δ) of the mean square charge radii of Strontium (Sr), Tin (Sn) and Lead (Pb) nuclei**

## 6.5. Nuclear Radii and Binding Energies Correlation

The difference of ms charge radii between pairs of even neutron number is plotted against neutron numbers, as called Brix-Kopfermann diagram, in Fig.6.6. The variation of two neutron separation energies S(2n) and the binding energy per nucleon are plotted for comparison, these values are taken from the compilation of Wapstra and Bos /Wap.77/. The increase in $\delta<r^2>$ of A=90 is associated with low value of S(2n) and a sudden decrease of the binding energy per nucleon.

A simple quantitative empirical correlation between relative variations of $<r^2>$ and differences in binding energies per nucleon has been observed by Gerstenkorn et.al. /Ger.60,Ger.69/. The relationship is expressed as, for a set of even neutron isotopes $A_o$ and $A_2$:

$$< r^2 >_2 - < r^2 >_o = -k_1(B_2 - B_o) + k_2 \tag{6.14}$$

where B is binding energy per nucleon, $k_1$ and $k_2$ are constant parameters. This relation allows the determination of the relative size of $<r^2>$ for various isotopes starting from the reliable measurements of binding energies. It does work well in particular for the isotopes with neutron number approaching the magic numbers. It was also expected that there exist anomalous ordering of $<r^2>$ as a function of mass number, i.e. inversion from the normally increasing function in strontium isotopes and included for Ti, Cr, Kr, Rb, Xe and Ce /Ger.79/.

Hefter et.al. /Hef.83, Hef.84/ have applied the inverse method to the solution of the nuclear mean field Schroedinger eigenvalue problem and yielded the simple relation:

$$\delta < r^2 > = 7.34(A^{2/3}/B(A) - A_0^{2/3}/B(A_0)) \tag{6.15}$$

where r is nuclear radius and B(A) is binding energy per nucleon of isotope A. This relation is also limited on the range of applicability due to the exclusion of shell effects and the existence of deformed nuclei is ignored.

The linear dependence of residual isotope shifts (the optical isotope shift minus its normal mass shift) to $\delta$(B/A) for corresponding pairs of even neutrons for xenon and barium had been studied by Wenz et.al./Wen.80/. The last pairs, involving the magic neutron number N=82, are the exception to the Gerstenkorn relation. They suggested that the shell closure effect should be taken into account by adding a term containing the Kronecker delta $\delta_{N,N-2}$ to the expression. By applying the plot of residual isotope shift variation from the optical data of krypton isotopes versus the difference of binding energy per nucleon, Gerhardt et.al./Ger.79/ could estimate the specific mass shift (SMS). As assuming the slope $k_1 = 0$ due to the small value of $<r^2>$ difference, the SMS of krypton could be evaluated from the intersection of the straight line at $\delta(B/A) = 0$, and was found to be approximately –2 MHz.

The strontium isotopes approaching N=50 are particularly suited to check these ideas. By plotting $\delta<r^2>^{N,N+2}$ versus $\delta(B/A)^{N,N+2}$, the two parameters are extracted to be $k_1 = 0.188$ fm$^2$/GeV and $k_2 = -0.068$ fm$^2$. From the plot of the residual isotope shift (RIS) differences against $\delta(B/A)$, we can extracted two parameters $k_1$ and $k_2$ to be 0.08 MHz/MeV and –97 MHz, respectively. Comparing to the extracted SMS value –31.75 MHz of strontium (N=48/50) the Gerhardt's concept fails to reproduce SMS in this case. It should be somewhat more complicated than such a simple relation proposed, for which up to now no theoretical explanation can be given.

A more refined analysis for the global trend of rms charge radii /Ang.77/ coupled to the trend of neutron separation energies /Nir.78/ has been made Angeli and Lombard /Ang.86/ to establish a correlation between variations of nuclear radii and binding energies. The first observation /Ang.77/, the deviation of experimental rms charge radii from the rough $A^{1/3}$ dependence shows simple trend of straight lines and varies systematically as a function of neutron number. The observed discontinuities between the straight lines can be explained qualitatively by the shell model. Whereas the second observation /Nir.78/, D. Nir has investigated the experimental results of mass measurements using a semiempirical mass formula. The analysis indicated that the existence of a universal dependence on neutron number for the shell effect term in the two neutron separation energies as the expression:

$$\beta = \Delta_{2N}(B_{exp}/B_s).8A \tag{6.16}$$

where $B_{exp}$ is the experimental binding energy, $B_s$ is calculated from a semiempirical formula and $\Delta_{2N}$ denotes the change of neutron number by 2 units. Combination of the two above mentions, the actual correlation between the variation of the nuclear radii and the binding energies could be established as the expression:

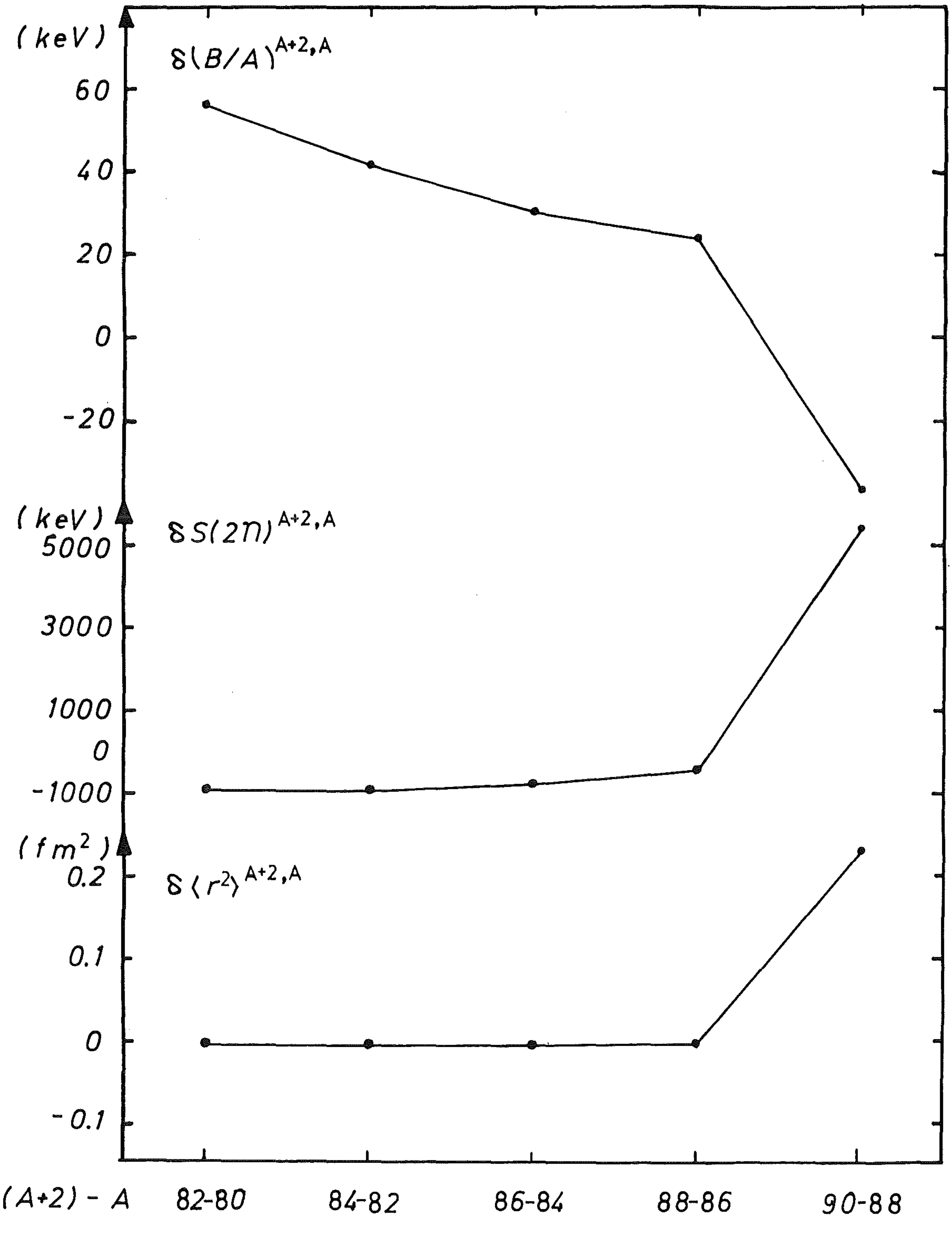

**Fig. 6.7** The plots of Brix–Kopfermann Diagram , the two neutron separation energies and the binding energy per nucleon /Wap.77/ with differences between two even A isotopes

$$\Delta r^2 = 2(f + 1/3)\Delta N.(r_o A^{1/3})^2/A \qquad (6.17)$$

**where $\Delta r^2$ is the square nuclear radius difference by $\Delta N$ neutron unit, $r_o$ = 1.2 fm and A is an atomic mass number. The quantity f is a three parameter function depending on neutron number and binding energy per nucleon as described above. This correlation is shown to be rather successful in predicting the global differences in nuclear radii but the discrepancies at some local such as $N < 50$ strontium isotopes, the concept of nuclear deformations should be accounted for.**

## 6.6. Nuclear Magnetic Dipole Moments

### 6.6.1. Schmidt Values

The extracted nuclear magnetic moments of strontium nuclei from these experimental results and the neighboring elements compiled by Lederer and Shirley /Led.78/ are plotted in the Schmidt diagram as shown in Fig.6.8. The plot of nuclear magnetic moments against the total nuclear spins shows the relationship to be expected in the single particle model of the nucleus, in which the nuclear properties are attributed to the effect of one nucleon. Strontium nuclei have the even proton number $Z = 38$ , hence most magnetic moments can be understood as arising from a single unpaired neutron. Most of the points observed experimentally of the nuclear magnetic moments lie between the Schmidt limits, the lower limit value −1.913 nm and the upper limit value equal to $+1.913\ I/(I+1)$ nm, where I is the total nuclear spin.

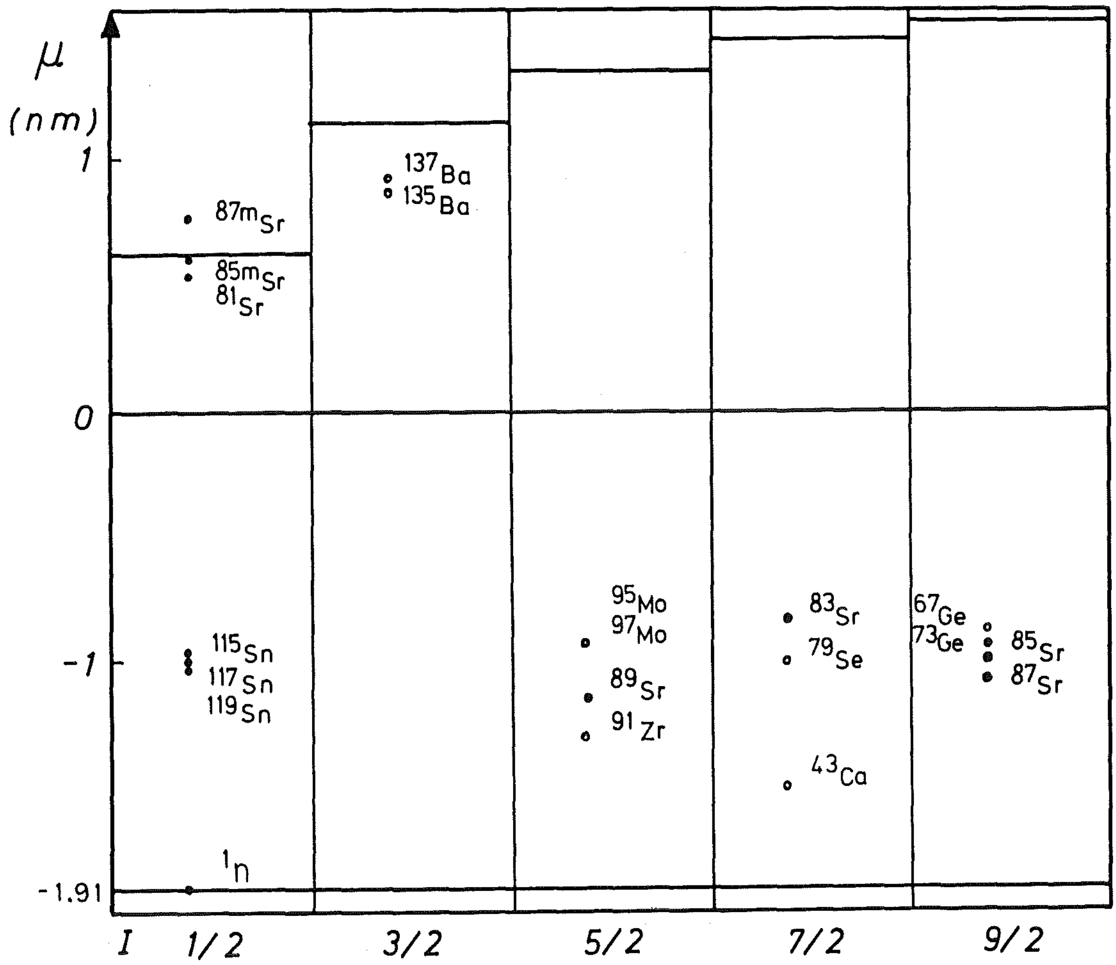

**Fig. 6.8** The deduced magnetic dipole moment values for the odd A – even Z nuclei in the Schmidt lines

The strontium nuclei with nuclear spin I = 1/2 (A = 81,85m and 87m) have the neutron configuration $(2p_{1/2})^1$. These nuclear magnetic moments lie nearly on the Schmidt value of +0.638 nm. Only the 87m value of +0.787 nm is observed to be slightly higher than the Schmidt value. It might be due to the fact that only one neutron is required to complete this shell. The ground state spins I = 9/2 of $^{85}$Sr and $^{87}$Sr belong to the neutron configurations $(1g_{9/2})^7$ and $(1g_{9/2})^9$ , respectively, with the Schmidt value of −1.913 nm for both isotopes. The actually observed values of the magnetic moments are around −1 nm, i.e. about half of the Schmidt limit as in many other neighbouring elements plotted in this diagram. Nearly the same value is observed for $^{89}$Sr with its ground state spin I = 5/2 and the neutron state of $(2d_{5/2})^1$. The single neutron lies after the closed shell of magic number N = 50. The discrepancy between the experimental data and the theory of Schmidt limit is due to the simplicity of the shell model that is based on a spherical symmetric potential, in reality nuclei are deformed. The other possible reason is that the magnetic dipole moments of the nucleons in nuclear matter differ from the free state due to the effect of the meson cloud changed around the nucleons.

### 6.6.2. Anomalous Coupling State

The nucleus of $^{83}$Sr is an irregular case. Its nucleus would be predicted from the single particle version of the shell model to have the the spin 9/2 or 1/2 corresponding to the assignment of the last unpaired neutron to a $g_{9/2}$ or possibly a $p_{1/2}$ orbital The observed spin I = 7/2 makes this $^{83}$Sr an exceptional nucleus /Lip.76/. The ground state of this N = 45 nucleus has been assigned $(g_{9/2})^{-3}_{7/2}$ with three holes in the $g_{9/2}$ orbital. Its seven $g_{9/2}$ neutrons contribute to coupling the total spin I = 7/2. Such an anomalous coupling of 45 neutrons also occurs in the ground states of the isotonic nuclei; $^{77}$Ge, $^{79}$Se and $^{81}$Kr, which all have $1g_{9/2}$ neutrons forming a nuclear spin 7/2 /Led.78/. This state has been called Kurath anomalous coupling state /Kop.56/, which is associated with the opposite parity state of a large spin in the major shell and there will appear an extra low-lying state swith spin I = (j-1). The anomalous coupling is discussed as arising from different effects. D. Kurath /Kur.50, Kur.52, Kur.53/ has considered finite range interactions to account for the anomaly for three nucleons or holes in a shell. L.S. Kisslinger /Kis.66/ described such $(j)^3_{j-1}$ states as caused by pairing plus a quadrupole interaction which sometimes considerably lowers these levels ( intruder–states ), in the present case of $^{83}$Sr down to the nuclear ground state. A. Kuriyama et.al. /Kur.72, Kur.73/ have further refined the model by introducing the "dressed" three quasiparticle modes.

The $^{83}$Sr can be understood as a $(1g_{9/2})^{-3}_{7/2}$ anomalous coupling state since the typical properties of such states are found. The competition between the regular I=9/2 and the I=7/2 anomalous coupling are demonstrated in $^{83}$Sr and $^{85}$Sr: in $^{85}$Sr the ground state still is I=9/2 and the 7/2 state lies 0.23 MeV above /Led.78/, whereas in $^{83}$Sr the two states are inverted. The change from A=85 to A=83 is accompanied by the continued increase of deformation as is expected from the above mentioned models /Kis.66, Kur.72/. In particular, the large positive quadrupole moment of $^{83}$Sr is a characteristic property of anomalous coupling as suggested by Hardy et.al. /Har.53/. They had measured the moments of $^{79}$Se (N=45), the isotonic nucleus of $^{83}$Sr and obtained $\mu(^{79}\mathrm{Se}) = -1.015$ nm and $Q_s(^{79}\mathrm{Se}) = +0.7(1)$ b. The measured magnetic moment was in agreement with the Schmidt value –1.50 nm calculated from a configuration of $j=l+1/2$ $(g_{9/2})$ neutrons.

### 6.6.3. Hyperfine Anomaly

Little can be said about the hyperfine anomaly. There is considerable $g_I$ value which predicted by the theory is that $g_I = \mu_I \ / \ (I.\mu_N)$. The $g_I$ values deduced from this experimental results are –0.2368(2) : $^{83}$Sr, –0.2220(2) : $^{85}$Sr and –0.2428(2) : $^{87}$Sr which are in good agreement with the $g_I$ value predicted by Kuriyama et.al. /Kur.72/ to be –0.24 nm. There is not any experimentally observed $g_I$ values because it is only one odd A (A=87) for the natural strontium isotopes, we can not deduced any hyperfine anomaly from our observed magnetic hyperfine constant (A) and $\mu_I$ values. But it is remarkable that the magnetic hyperfine constant ratio A(87) / A(85) = 1.093(3) and the ratio of $\mu/I$ for isotopes 85:83 = 0.9376(9). Comparing to the data of krypton, the neighboring element, as reported by Gerhardt et.al. /Ger.81/ , it resulted that the ratio of magnetic moments $\mu(^{85}\mathrm{Kr}) \ / \ \mu(^{83}\mathrm{Kr}) = 1.030(2)$ and for the quadrupole moments $Q(^{83}\mathrm{Kr}) \ / \ Q(^{85}\mathrm{Kr}) = 1.712(9)$. It is surprising, since both lie in the same $g_{9/2}$ neutron state and not so far from the major neutron magic number N = 50. They suggested that the great difference of quadrupole moments induced the hyperfine anomaly between these two nuclei.

## 6.7. Nuclear Electric Quadrupole Moments

The extracted values of electric quadrupole moments ($Q_s$) of the strontium nuclei are shown in Table 5.6 and plotted in Fig.6.9. The spectroscopic quadrupole moments for strontium A=85 and 87 show the positive values and quite the same magnitude of +0.335(20) b and +0.32(2) b, respectively. For A=83, $Q_s$ is +0.82(5) b, the suddenly large value reflects a drastic change of nuclear deformation between the isotopes A=83 and 85. The $Q_s$ of A=81 nucleus can not be derived from this experimental data, due to its ground state spin I=1/2 and is excluded for the $Q_s$ value from the Casimir formula. In this plot we let the zero value of $Q_s(81)$ in order to guide the eyes. The negative value of $Q_s(89) = -0.30(3)$ b means that the oblate form nucleus was occured after adding one neutron to the spherical $^{88}$Sr nucleus.

The spectroscopic quadrupole moment $Q_s$ is proportional to the B factor. In the case where the nucleus is axially symmetrical and strongly deformed, the intrinsic quadrupole moment $Q_o$ may be obtained by the projection formula: $Q_o = Q_s\ (I+1)(2I+3)\ /\ I(2I-1)$. The results of $Q_o$ values are also plotted in Fig.6.9. However, the strontium nuclei appear to be transitional so that such a simple relation $Q_o$ and $Q_s$ is not very realistic.

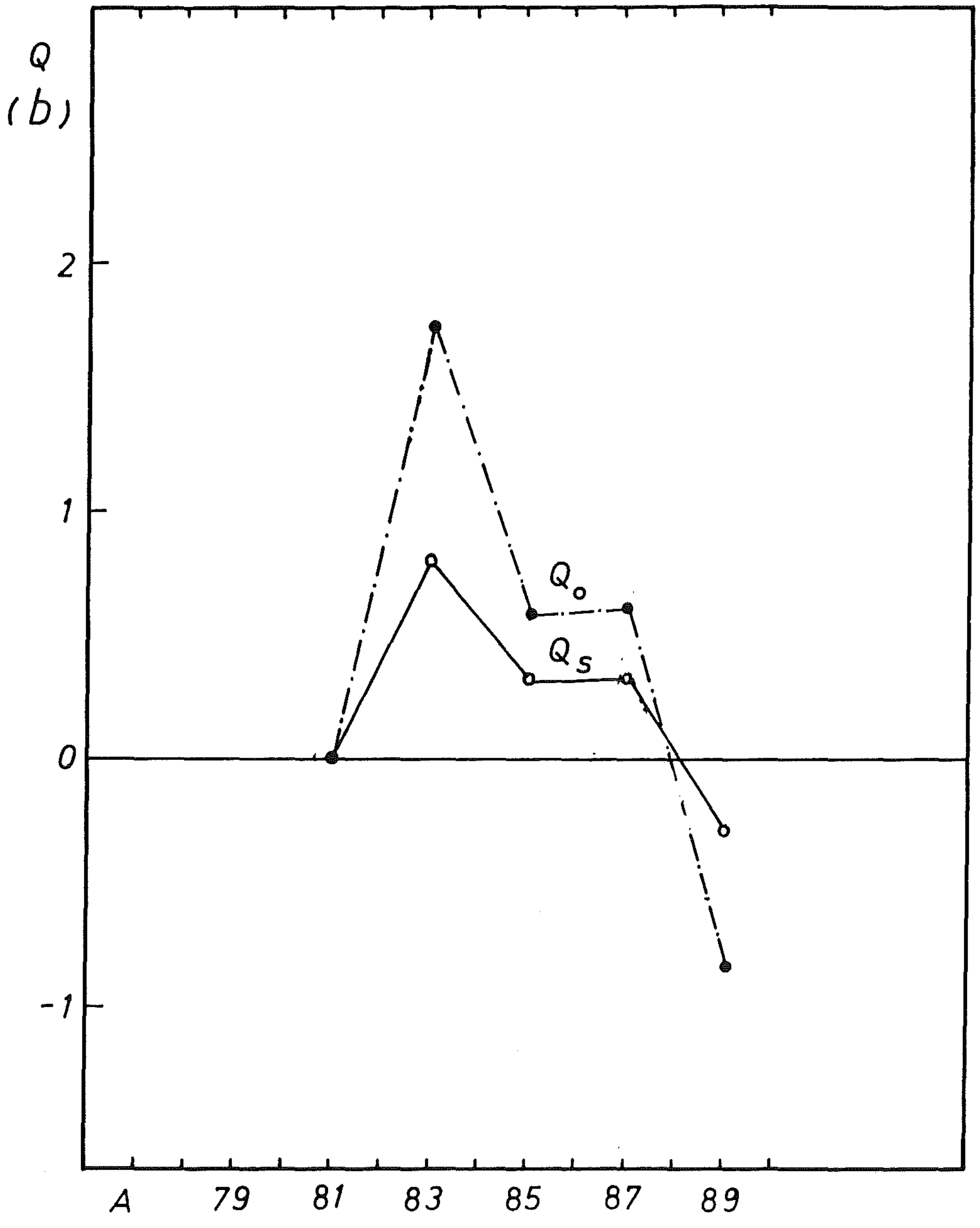

**Fig. 6.9** The spectroscopic quadrupole moments ($Q_s$) the intrinsic quadrupole moments ($Q_o$)

## 7. CONCLUSION

An attempt has been made on measuring the isotope shifts and the hyperfine splittings for a long isotopic chain of strontium A = 80 – 90, including two isomers 85m and 87m. The method was based on the resonance excitation of a collimated atomic beam by using a laser beam crossing at right angle. The 293.2 nm uv light was achieved by the second harmonic generation method with either a temperature tuned ADA crystal or an angle tuned $LiIO_3$ crystal. The induced atomic transition is $5s^2\ ^1S_0 - 5s6p\ ^1P^1$ and the emitted photon of 716.7 nm from decaying to the $5s4d\ ^1D_2$ metastable state were observed. The neutron deficient isotopes ( A = 80,81,82,83,85m ) were produced by alpha induced reactions ( $\alpha$, xn ) with enriched krypton gas targets, whereas the long half-life ( A=85 ) and the neutron riched isotopes ( A = 89,90 ) were purchased as a nitrate solutions. Purified isotopes were available by an electromagnetic mass separator and the least amount used was about 60 pg. The rf side-band method was employed for laser frequency scanning and control with high precision.

The experimental results of the isotope shifts and the hyperfine interactions give important information on the particular nucleus which can be extracted as the following summary.

1. The variation of ms charge radii are evaluated from the measured isotope shifts by the King plot procedure using the muonic X-ray data coupled with the extracted $\delta\langle r^2\rangle$ values from some optical data. The kink of $\langle r^2\rangle$ value at N=50 shows a distinct closed shell effect.

2. The negative shift of $\delta\langle r^2\rangle$ is the increase of radii with decreasing neutron number below N=50, which is ascribed to an increasing deformation. Applying the simple two parameter droplet model, the extracted deformation parameters show consistent with the values from $B(E2,0^+-2^+)$ results.

3. The charge radius of the isomeric nucleus 85m is lying well in the middle of the neighboring even nuclei and is greater than its ground state nucleus, which is in contrasted to 87m.

4. An inverse odd-even staggering occurs from A=83 through the lower mass number nuclei in contrasting to the normal odd-even staggering effect, where the odd nuclei are always slightly smaller than the average of the even neighbours. They supported somewhat the evidence that A=84 nucleus is the border between the spherical and the deformed nuclei as shown by the

gamma ray spectroscopic methods. The staggering parameter of A=89 nucleus is nearly unity which supports the idea that the magic plus one nuclei are very little deformed.

5. The correlation between relative variation of $<r^2>$ and differences in binding energy per nucleon and the differences in two neutron separation energies is limited on the range of applicability due to the exclusion of shell effect and the existence of deformed nuclei for strontium A $<$ 88 is ignored.

6. The isotonic comparison of $\delta<r^2>$ values between the neighbouring elements Krypton (Z=36), Rubidium (Z=37), Strontium (Z=38), Zirconium (Z=40) and Molybdenum (Z=42) show nearly the same trends for both sides of the closed shell.

7. The actually observed values of the magnetic dipole moments of odd A isotopes (A=83,85,87) are around $-1\mu_N$, i.e. about half of the Schmidt value, whereas the I=1/2 isomeric nucleus (A=87m) is larger than the Schmidt value ($+0.638\mu_N$).

8. The large electric quadrupole moment and the relation of the magnetic dipole moments are supporting the behavior of the Kurath anomalous coupling state of $^{83}$Sr in which the ground state can well be understood as a $\nu(1g_{9/2})^{-3}_{7/2}$ intruder state.

9. The spectroscopic quadrupole moments of A=83,85 and 87 show the evolution of the nuclear deformation in prolate shapes when going away from A=88 nucleus, while A=89 nucleus reveals an oblate shape.

# REFERENCES

And.82 Andl, A., Bekk, K., Göring, S., Hanser, A., Meisel, G., Rebel, H., Schatz, G. and Thompson, R.C.: Phys. Rev. C26 (1982) 2194

Ang.77 Angeli, I. and Csatlos, M.: Nucl. Phys. A288 (1977) 480

Ang.78 Angeli, I. and Csatlos, M.: ATOMKI Kozl. 20 (1978) 1

Ang.86 Angeli, I. and Lombard, R.J.: Z. Phys. A324 (1986) 299

Ans.83 Anselment, M., Chongkum, S., Hoeffgen, H. J. and Meisel, G.: Ann. Rep. Nucl. Phys. Act. KfK. 3621 (1983) 65

Ans.85 Anselment, M., Chongkum, S., Göring, S., Hanser, A., Meisel, G., Rebel, H. and Schatz, G.: Ann. Rep. Nucl. Phys. Act. KfK 3969 (1985) 63

Ans.86 Anselment, M., Chongkum, S., Göring, S., Hanser, A., Meisel, G. and Rebel, H.: Z. Phys. D 3 (1986) 421

Ans.86a Anselment, M., Faubel, W., Göring, S., Hanser, A., Meisel, G., Rebel, H. and Schatz, G.: Nucl. Phys. A451 (1986) 471

Ans.86b Anselment, M., Bekk, K., Göring, S., Hanser, A., Hoeffgen, H., Meisel, G., Rebel, H. and Schatz, G.: Phys. Rev. C34 (1986) 1052

Ans.87 Anselment, M., Bekk, K., Chongkum, S., Göring, S., Hanser, A., Hoeffgen, H. J., Kälber, W., Meisel, G., and Rebel, H.: Z. Phys. A326 (1987),in press

Asp.84 Aspect, A., Bauche, J., Fonseca, A. L. A., Grangier, P. and Roger, G.: J. Phys. B. At. Mol. Phys. 17 (1984) 1761

Auf.78 Aufmuth, P., Clieves, H.P., Heilig, K., Steudel, A. and Wendlandt, D.: Z. Phys. A285 (1978) 357

Auf.82 Aufmuth, P.: J. Phys. B15 (1982) 3127

Auf.83 Aufmuth, P. and Haunert, M.: Physica 123C (1983) 109

Bab.62 Babushkin, F. A.: Sov. Phys. JETP 15 (1962) 1113

Bab.63 Babushkin, F. A.: Sov. Phys. JETP 17 (1963) 1118

Ban.73 Banck, J. and Schwenk, A.: Z. Phys. 265 (1973) 165

Bau.76 Bauche J. and Champeau R. J.: Adv. At. Mol. Phys. 12 (1976) 39

Bei.83 Beigang, R., Makat, W., Timmermann, A. and West, P. J.: Phys. Rev. Lett. 51 (1983) 771

Bek.79 Bekk, K., Andl, A., Göring, S., Hanser, A., Nowicki, , G., Rebel, H. and Schatz, G.: Z. Phys. A291 (1979) 219

Ben.84 Bender D., Brand H. and Pfeufer V.: Z. Phys. A318 (1984) 291

Ben.84a Bengtsson, R., Möller, P., Nix, J. R. and Zhang, J. Y. : : Physica Scripta 29 (1984) 402

Bli.78 Blit, S., Weaver, E. G., Rabson, T. A. and Tittel, F. K. : App. Optics 17 (1978) 721

Blu.85 Blundell, S. A., Baird, P. E. G., Palmer, C. W. P., Stacey, D. N., Woodgate, G. K. and Zimmermann, D.: Z. Phys. A321 (1985) 31

Blo.85 Blomqvist, J. and Rydström, L. Physica Scripta 31 (1985) 31

Bod.54 Bodmer, A. R.: Proc. Phys. Soc. A67 (1954) 622

Boe.74 Boehm F. and Lee P. L.: At. Data Nucl. Data Tables 14 (1974) 6

Boh.50 Bohr, A. and Weisskopf, V. F.: Phys. Rev. 77 (1950) 94

Boh.75 Bohr, A. and Mottelson, B. R.: Nuclear Structure, vol.II W.A. Benjamin Inc., Reading, Mass. (1975)

Bor.83 Borghs, G., Bisschop, D. P., Hove M.V. and Silverans, R. E.: Hyperfine Interaction 15/16 (1983) 177

Boy.68 Boyd, G. D. and Kleinman, D. A.: J. of Appl. Phys. 39 (1968) 3597

Bre.31 Breit, G.: Phys. Rev.: 38 (1931) 463

Bri.52 Brix, P. and Kopfermann H.: Z. Phys. 133 (1952) 192

Bro.84 Brown, B. A., Bronk, C. R., and Hodgson, P. E., J. Phys. G. Nucl. Phys. 10 (1984) 1683

Bru.69 Bruch, R., Heilig, K., Kaletta, D., Steudel, A. and Wendlandt, D.: J. Phys.(Paris) 30 (1969) Suppl. C1-51

Buc.85 Buchinger, F., Corriveau, R. and Ramsay, E. B.: Phys. Rev. C32 (1985) 2058

Bue.86 Buesener, H., Renn, A., Brieger, M., von Moers, F. and Hese, A.: Appl. Phys. B39 (1986) 77

Bun.76 Bunting, R. L. and Kraushaar, J. J.: Nuclear Data Sheets 18 (1976) 87

Bur.79 Burghardt, B., Jitschin, W. and Meisel, G.: Appl. Phys. 20 (1979) 141

Büt.82 Büttgenbach, S.: Hyperfine Structure in 4d and 5d Shell Atom, Springer tracks in Modern Physics vol.96, Springer- Verlag Berlin, Heidelberg, New York. (1982)

Büt.84 Büttgenbach, S.: Hyperfine Interactions 20 (1984) 1

Cam.80 Campi, X. and Epherre, M.: Phys. Rev. C22 (1980) 2605

Cas.36 Casimir, H.: Teylors Tweede Genootshap 1 (1936) 11

Chr.72 Christy, A. and Häusser, O.: Nucl. Data Tables 11 (1972) 281

Col.67 Collard, H. R., Elton, L. R. B. and Hofstadter, R.: ”Nuclear Radii” in Landolt-Börnstein, group I vol. 2, ed. H. Schopper ,Springer-Berlin, (1967) 5

Cor.77 Corney, A.: ”Atomic and Laser Spectroscopy”, Clarendon Press. Oxford (1977)

Cou.81 Couilloud, B.: J. de Phy. Col. C8 (1981) 115

Cow.81 Cowan, R. D.: The Theory of Atomic Structure and Spectra, University of California Press, Berkeley (1981)

Dem.80 Demtröder W.: ”Laser Spectroscopy”, Springer-Verlag Berlin Heidelberg New York (1980)

Dew.82 Dewald, A., Kaup, U., Gast, W., Gelberg, A., Schuh, H. W., Zell, K. O. and Brentano, P. von.: Phys. Rev. C25 (1982) 226

Eas.86 Eastham, D. A., Walker, P. M., Smith, J. R. H., Griffith, J. A. R., Evans, D. E., Well, S. A., Fawcett, M. J. and Grant, I. S.: J. Phys. G: Nucl. Phys. 12 (1986) L205

Eas.87 Eastham, D. A., Walker, P. M., Smith, J. R. H., Warner, D. D., Griffith, J. A. R., Evans, D. E., Wells, S. A., Fawcett, M. J. and Grant, I. S., to be submitted to Phys. Rev. Lett.

Ehr.68 Ehrlich, R. D.: Phys. Rev. 173 (1968) 1088

Eli.83 Eliel E. R. and Hogervorst, W.: Z.Phys. A311 (1983) 1

Emr.81 Emrich H. J., Fricke J., Hosen M., Kaser K., Mallot M., M Miska, S., Robert-tissot, B., Rychel, D., Schaller, L., Schneawly, H., Shera, B., Sieberling, H. G., Steffen, R., Wohlfahrt, H. D., and Yamazaki, Y.: Proc. 4th Int. Conf. on Nuclei Far From Stability, Helsingor, Denmark, June 7-13,1981, vol 1,33.

Eng.74 Engfer, R., Schneuwly, H., Vuilleumier, J. L., Walter, H. K., Zehnder, A.: At. Data Nuc. Data Tables 14 (1974) 509

Eph.81 Epherre, M., Audi, G. and Campi, X.: 4th. Int. Conf. on Nuclei far from Stability, Helsingor, CERN 81-09 (1981) 63

Fab.65 Fabricius, H., Freitag, K. and Göring, S.: Nucl. Instr. and Meth. 38 (1965) 64

Fab.66 Fabricius, H., Freitag, K., Göring, S., Hanser, A, and Langmann, H.J.: KfK report 511 (1966)

Fer.33 Fermi, E. and Segre, E.: Z. Phys. 82 (1933) 729

Feu.78 Feurer, B. and Hanser, A.: KfK report no. 2682 (1978) 72

Fie.81 Fields, C. A., Boer, F. W. N. de., Sugarbaker, E. and Walker, P.M.: Nucl. Phys. A363 (1981) 352

Foo.84 Foot, C. J., Baird, P. E. G., Bosbier, M. G., Stacey, D. N., Woodgate, G.K.: Opt. Com. 50 (1984) 199

Fra.62 Fradkin, E. E.: Sov. Phys. JETP 15 (1962) 550

Fri.86 Fricke, G.: Private communication (1986)

Frö.76 Fröhlich, D., Stein, L. and Schröder, H. W.: Appl. Phys. 11 (1976) 17

Ful.69 Fuller, G. H. and Cohen, V. W.: Nucl. Data Tables A5 (1969) 433

Gal.86 Galeriu, D., Bucurescu, D. and Ivascu, M.: J. Phys. G: Nucl. Phys. 12 (1986) 329

Gau.33 Gaudsmit, S.: Phys. Rev. 43 (1933) 636

Ger.79a Gerhardt, H., Matthias, E., Rinneberg, H., Schneider, F. , Timmermann, A., Wenz, R., and West, P.J.: Z. Phys. A292 (1979) 7

Ger.81 Gerhardt, H., Jeschonnek, F., Makat, W., Matthias, E., Rinneberg, H., Schneider, F., Timmermann, A. and West, P. J.: Hyperfine Interactions 9 (1981) 175

Ger.60 Gerstenkorn, S.: C.R. Acad. Sci. 250 (1960) 825

Ger.69 Gerstenkorn, S.: C.R. Acad. Sci. B268 (1969) 1636

Ger.78 Gerstenkorn, S. and Luc, P.: "Atlas du Spectre d' Absorption de la Molecule d' Iode", ed du Centre National de la Recherche Scientifique, Paris (1978)

Ger.79 Gerstenkorn, S.: Comm. Atom and Mol. Phys. D9 (1979) 1

Gro.62 Grodzins, L.: Phys. Lett. 2 (1962) 88

Gru.83 Grundevik P., Gustavsson M., Lindgren I., Olsson G., Olsson, T. and Rosen A.: Z. Phys. A311 (1983) 143

Ham.81 Hamilton, et. al. IV Cof. on Nuclei Far From Stability, CERN 81-09 (1981) 391

Ham.84 Hamilton, J. H., Ramayya. A. V., Maguire, C. F., Piercey, R. B., Bengtsson, R., Moller, P., Nix. J. R., Zhang J. Y., Robinson, R. L., and Frauendorf, S.: J Phys G.: Nucl. Phy.10 (1984) L87

Ham.85 Harminton, J. H.: Prog. in Particles and Nuclear Physics. vol.15 (1985) 107

Har.53 Hardy, W. A., Silvey, G., Townes, C. H., Burke, B. F., Strandberg, M. W. P., Parker, G. W., Cohen, V. W.: Phys. Rev. 92 (1953) 1532

Has.85 Haskins, P. S., Dunnam, F. E., Coldwell, R. L.,Rester, A. C., Piercey, R. B., Muga, M. L., Rinsvelt,H. A. van, Smart, R. W., Aarts, H. J. M., Fox, J. D., Dennis, L. C. and Saw, C. B.: Phys. Rev. C32 (1985) 1897

Hef.83 Hefter, E. F. and Gridnev, K. A.: Z. Naturforsch. 38a (1983) 813

Hef.84 Hefter, E. F., Llano, M. de. and Mitropolski,I. A.: Phys. Rev. C30 (1984) 2042

Hei.61 Heilig K.: Z. Phys. 161 (1961) 252

Hei.63 Heilig, K., Schmitz, K. and Steudel, A.: Z. Phys. A176 (1963) 120

Hei.74 Heilig, K.and Steudel, A.: At. Data Nucl. Data Tables 14 (1974) 613

Hei.77 Heider, S. M. and Brink G.O .: Phys. Rev. A16 (1977) 1371

Hey.84 Heyde, K., Moreau, J. and Waroquier, M.: Phys. Rev. C29 (1984) 1859

Hig.83 Higo, T., Matsuki, S. and Yanabu, T.: Nucl. Phys. A393 (1983) 224

Hug.57 Hughes R. H.: Phys. Rev. 105 (1957) 1260

Hul.64 Hulpke, E., Paul, E. and Paul, W.: Z. Phys. 177 (1964) 257

Jön.84 Jönsson, G., Levison, C., Persson, A. and Wahlstrom C. G. : Phys. A316 (1984) 255

Kin.63 King, W. H.: J. Opt. Soc. Am. 53 (1963) 638

Kin.84 King, W. H.: "Isotope Shift in Atomic Spectra", Plenum Press N.Y. (1984)

Kis.66 Kisslinger, L. S.: Nucl. Phys. 78 (1966) 341

Klu.74 Kluge, H. J. and Sauter, H.: Z.Phys. 270 (1974) 295

Kop.58 Kopfermann, H.: "Nuclear Moments" Academic, New York (1958)

Kuc.58 Kucheriaev, A. G., Szhenov, I. K., Gogichaishvili, S. M., Leont'eva, I. N. and Vasil'ev, L. V.: Soviet Phys. JETP 7 (1958) 533

Kuc.59 Kucheriaev, A. G., Szhenov, Y. K. and Gogichaishvili, S. M.: Soviet Phys. JETP 8 (1959) 412

Kuh.69 Kuhn, H. G.: "Atomic Spectra", Longmans 2nd. ed. (1969)

Kur.50 Kurath. D.: Phys. Rev. 80 (1950) 98

Kur.52 Kurath. D.: Phys. Rev. 88 (1952) 804

Kur.53 Kurath. D.: Phys. Rev. 91 (1953) 1430

Kur.72 Kuriyama, A., Marumori, T., Matsuyanagi, K.: Prog. Theor. Phys. 47 (1972) 498

Kur.73 Kuriyama, A., Marumori, T., Matsuyanagi, K.: J. Phys. Soc Jap. Suppl. 34 (1973) 34

Led.78 Lederer, C. M. and Shirley, V. S.: Tables of Isotopes Wiley and Sons Inc. New York (1978)

Lee.73 Lee, P. L. and Boehm, F.: Phys. Rev. C8 (1973) 819

Lia.82 Liang, C. F., Paris, P., Bucurescu, D., Della Negra, S., Obert, J. and Putaux, J.C.: Z. Phys. A309 (1982) 185

Lip.76 Liptak, J., Kristiak, J. and Kristiakova, K.: Czech. J. Phys. B26 (1976) 1321

Lis.79 Lister, C. J., Haustein, P. E., Alburger, D. E. and Olness, J. W.: Bull. Am. Phys. Soc. Ser.II 24 (1979) 826

Lis.82 Lister, C. J., Varley, B. J., Price, H. G., and Olness, J.: Phys. Rev. Lett. 49/5 (1982) 308

Löb.70 Löbner, K. E. G., Vetter, M. and Honig, V.: Nucl. Data Tables A7 (1970) 495

Lor.82 Lorenzen, C. J. and Niemax, K.: Opt. Commun. 43 (1982) 26

Lor.83 Lorenzen, C. J., Niemax, K. and Pendrill, L.R.: Phys. Rev. A28 (1983) 2051

Mar.80 Marshall, C. M.: App. Optics 19 (1980) 1980

Mar.86 Martin, A. G., Dutta, S. B., Rogers, W. F., Clark, D. L.: Phys. Rev. C34 (1986) 1120

Meg.75 Meggers, W. F., Corliss, C. H., Scribner, B. F.: Tables of Sprectral Line Intensities, NBS.(U.S.) Circ.No.145 U. S. GPO, Washington, D.C., 1975

Möl.81 Möller, P. and Nix, J. R.: Atom. Data and Nucl. Data Tables 26 (1981) 165

Moo.71 Moore, C. E.: "Atomic Energy Levels", Nat. Stand. Ref. Data Ser., Nat. Bur. Stand.(US), 35/vol.2 (1971)

**Mül.79** Müller, H. W. and Tepel, J. W.: Nuclear Data Sheets 27 (1979) 399

**Mye.77** Myers, W. D. ”Droplet Model of the Nucleus”, IFI/Plenum Data Co. New York (1977)

**Mye.80** Myers, W. D. and Swiatecki, W. J.: Nucl. Phys. A336 (1980) 267

**Mye.83** Myers, W. D. and Schmidt, K. H.: Nucl. Phys. A410 (1983) 61

**Nat.69** Nath, G. and Haussuhl, K.: App. Phys. Lett. 14 (1969) 154

**Naz.85** Nazarewicz, W., Dudek, J., Bengtsson, R., Bengtsson, T. and Ragnarsson, I.: Nucl. Phys. A435 (1985) 397

**Nir.78** Nir, D.: Phys. Rev. C18 (1978) 1022

**Nol.74** Nolte, E., Shida, Y., Kutschera, W., Prestele, R. and Morinaga, H.: Z.Phys. 268 (1974) 267

**Ols.72** Olschewski, L.: Z. Phys. 249 (1972) 205

**Pie.81** Piercey, R. B., Hamilton, J. H., Soundranayagam, R., Ramayya, A. V., Maguire, C. F., Sun, X. J., Zhao, Z. Z., Robinson, R. L., Kim, H. J., Frauendorf, S., Döring, J., Funke, L., Winter, G., Roth, R. L., Cleemann, L., Eberth, J., Neumann, W., Wells, J. C., Lin, J., Rester, A. C. and Carter, H. K.: Phys. Rev. Lett. 47 (1981) 1514

**Rag.84** Ragnarsson, I. and Sheline, R.K.: Physica Scripta 29 (1984) 385

**Reb.82** Rebel, H. and Schatz, G., Conf. on Laser in Nuclear Physics, Apr 21-23,1982 Oak Ridge, Tennessee, U.S.A.

**Ree.71** Reehal, B. S. and Sorensen, R. A.: Nucl. Phys. A161 (1971) 385

**Ros.32** Rosenthal, J. E., and Breit, G.: Phys. Rev. 41 (1932) 459

**Sah.74** Sahm, W. and Schwenk, A.: Z. Naturforsch. 29A (1974) 1763

**Sch.80** Schatz, G.: unpublished report (1980)

**Sel.69** Seltzer, E. C.: Phys. Rev. 188 (1969) 1916

**Sob.72** Sobel'man, I. I.: ”An Introduction to the Theory of Atomic Spectra”, Pergamon Press. Oxford (1972)

**Sor.66** Sorensen, R. A.: Phys. Lett. 21 (1966) 333

**Sta.66** Stacey, D. N.: Rep. Prog. Phys. 29 (1966) 171

**Ste.84** Steiger, A.: KfK Report No. 3820 (1984)

**Ste.65** Stelson, P. H. and Grodzins, L.: Nucl. Data Tables A1 (1965) 21

**Ste.71** Sternheimer, R. M. and Peierls, R. F.:Phys. Rev. A3 (1971) 837

| | |
|---|---|
| Ste.74 | Sternheimer, R. M. and Peierls, R. F.:Phys. Rev. A9 (1974) 1783 |
| Swa.68 | Swagel, M. and Laurio, A.: Phys. Rev. 169 (1968) 114 |
| Tal.60 | Talmi, I. and Unna, I.: Nucl. phys. 19 (1960) 225 |
| Tal.84 | Talmi, I.: Nucl. Phys. A423 (1984) 189 |
| Tep.78 | Tepel, J. W.: Nuclear Data Sheets 25 (1978) 553 |
| Thi.81 | Thibault, C., Touchard, F., Büttgenbach, S., Klapisch, R., de Saint Simon, M., Duong, H. T., Jacquino, P., Juncar, P., Liberman, S., Pillet, P., Pinard, J., Vaille, J. L., Pesnelle, A. and Huber, G.: Phys. Rev. C23 (1981) 2720 |
| Tom.68 | Tomlinson, W. J. and Stroke, H. H.: Nucl. Phys. A161 (1968) 614 |
| Wap.77 | Wapstra, A. H. and Bos, K.: At. Data Nucl. Data Tables 19 (1977) 177 |
| Wei.35 | Weizsäcker, C. F. von.: Phys. Rev. 96 (1935) 431 |
| Wen.80 | Wenz, R., Matthias, E., Rinneberg, H., and Schneider, F.: Z. Phys. A295 (1980) 303 |
| Wes.85 | Wesolowski, E.: J. Phys. G: Nucl. Phys. 11 (1985) 909 |
| Wil.53 | Wilets, L., Hill, D. L. and Ford, K. W.: Phys. Rev. 91 (1953) 1488 |
| Yar.76 | Yariv, A.,"Quantum Electronics" 2.ed. John Wiley & Sons, Inc. USA (1975) |
| Zaw.80 | Zawischa, D.: Proc. Int. Conf. Nucl. Phys. (Berkley, 1980) p.734 |
| Zer.73 | Zernike, F. and Midwinter, J. E., "Applied Nonlinear Optics John Wiley & Sons, Inc. Canada (1973) |
| Zim.84 | Zimmermann, D., Z. Phys. A315 (1984) 123 |
| zuP.63 | zu Putlitz, G.: Z. Phys. 175 (1963) 543 |